A Route to Erbium-doped Nanocrystals as a Single Photon Source Using Double Nanohole Optical Tweezers

by

Michael DOBINSON
B.Eng., University of Victoria, 2018

A thesis submitted in partial fulfillment of the requirements
for the degree of

MASTER OF APPLIED SCIENCE

in the

Department of Electrical and Computer Engineering

We acknowledge with respect the lək̓ʷəŋən peoples on whose traditional territory the university stands and the Songhees, Esquimalt and W̱SÁNEĆ peoples whose historical relationships with the land continue to this day.

Supervisory Committee

A Route to Erbium-doped Nanocrystals as a Single Photon Source Using Double Nanohole Optical Tweezers

by

Michael DOBINSON

B.Eng., University of Victoria, 2018

Supervisory Committee

Dr. Reuven GORDON, **Supervisor**

Department of Electrical and Computer Engineering

Dr. Levi SMITH, **Committee Member**

Department of Electrical and Computer Engineering

Abstract

This thesis presents a route towards a single photon source based on erbium-doped nanocrystals, fabricated with methods that use double nanohole optical tweezers. Single photon sources are an exciting quantum technology and erbium is good candidate as it emits in the low-loss fiber optic C-band, but it is a weak emitter. Double nanohole apertures can be designed with plasmonic resonances to enhance the local electric field. In this thesis, double nanohole optical tweezers are used to isolate and enhance the emission of erbium-doped nanocrystals, with the tuned geometry showing a factor of 50 additional enhancement over rectangular apertures. With the enhanced emission, nanocrystals with discrete levels of erbium emitters are detected and isolated in real-time, based on their level of emission. This real-time process demonstrates a major improvement over typical post-processing approaches.

A novel method to anchor nanocrystals in a double nanohole using a photochemical thiol reaction was investigated which yielded 40% of nanoparticles anchoring within 2 µm of the DNH, with 5% inside. This is useful as otherwise the trapping laser must be maintained to keep the nanocrystal in the trap. Another challenge is coupling to an optical fiber, for which a method to combine trapping and coupling was explored. Colloidal pattern transfer is presented as a low-cost fabrication method for nanoaperture optical fiber tweezers, with fiber-based trapping demonstrated using 40 nm polystyrene nanospheres and hexagonal boron nitride. The preliminary results from these methods show great potential, and with further refinement they may lead towards a method to fabricate a low-cost fiber-coupled single photon source based on erbium-doped nanocrystals.

Table of Contents

List of Figures

List of Symbols

Symbol	Name	Unit
α	polarizability	$\mathrm{C\,m^2\,V^{-1}}$
α_c	attenuation	$\mathrm{dB\,km^{-1}}$
β	propagation constant	$\mathrm{rad\,m^{-1}}$
γ	decay rate	$\mathrm{s^{-1}}$
ε_0	vacuum permittivity	$\mathrm{F\,m^{-1}}$
ε_r	relative permittivity	(1)
η	quantum efficiency	(1)
λ	wavelength	m
μ_0	vacuum permeability	$\mathrm{H\,m^{-1}}$
μ_r	relative permeability	(1)
τ	time delay	s
ω	angular frequency	$\mathrm{rad\,s^{-1}}$
$\mathcal{C}$	counts	(1)
k	wavenumber	$\mathrm{m^{-1}}$
n	refractive index	(1)
P	power	W ($\mathrm{J\,s^{-1}}$)
Q	quality factor	(1)
t	time	s
T	transmission	(1)
r	radius	m
V	volume	$\mathrm{m^3}$
$\mathcal{V}$	HOM interference visibility	(1)
$\mathbf{E}$	electric field vector	$\mathrm{V\,m^{-1}}$
$\mathbf{p}$	dipole moment vector	C m
$\mathbf{r}$	position vector	m
∇	vector differential operator	–
$\langle\,\rangle$	time average	–
$\perp$	perpendicular	–
$\parallel$	parallel	–

Glossary

APD	**A**valanche **P**hoto**d**iode
CCD	**C**harge-**c**oupled **D**evice
CMOS	**C**omplementary **m**etal–**o**xide–**s**emiconductor
CW	**C**ontinuous **W**ave
DAQ	**D**ata **Ac**q**u**isition
DNH	**D**ouble **N**ano**h**ole
EDFA	**E**rbium-**D**oped **F**iber **A**mplifier
HBT	**H**anbury-**B**rown-**T**wiss
HOM	**H**ong-**O**u-**M**andel
HWP	**H**alf-**w**ave **P**late
IR	**I**nfra**r**ed
LP	**L**inear **P**olarizer
LPF	**L**ong-**p**ass **F**ilter
MMF	**M**ulti-**m**ode Optical **F**iber
NA	**N**umerical **A**perture
NAFT	**N**ano**a**perture Optical **F**iber **T**weezers
NIR	**N**ear-**i**nfra**r**ed
NP	**N**ano**p**article
pHP	***p*-h**ydroxy**p**henacyl
PVC	**P**oly**v**inyl **C**hloride
RMS	**R**oot **M**ean **S**quare
SEM	**S**canning **E**lectron **M**icroscope
SPF	**S**hort-**p**ass **F**ilter
SMF	**S**ingle-**m**ode Optical **F**iber
SNSPD	**S**uper-conducting **N**anowire **S**ingle **P**hoton **D**etector
UV	**U**ltra**v**iolet

Acknowledgements

I would first like to thank my supervisor, Dr. Reuven Gordon, whose valuable support and insight throughout my studies I greatly appreciate.

I am appreciative of my collaborators and colleagues in the Nanoplasmonics Research Group for their support and encouragement, including Zohreh Sharifi, Ghazal Hajisalem, Ryan Peck, Mirali Shariatdoust, Hao Zhang, Behnam Khosravi, and Elham Babaei. I would also like to thank my collaborators in the Department of Chemistry, Dr. Frank C.J.M. van Veggel and Adriaan Frencken.

I also am grateful for the training and support from the faculty and staff in the Centre for Advanced Materials and Related Technology (CAMTEC) and the Advanced Microscopy Facility (AMF).

Finally, I thank my family, my partner, and my friends for their motivation, love, and support.

Chapter 1

Introduction

This thesis focuses on a specific candidate for single photon sources, erbium-doped nanocrystals, and explores their optical properties and methods to enhance their emission using double nanohole (DNH) optical tweezers, a method to anchor the nanocrystals within a DNH, and a method to fabricate nanoaperture fiber tweezers (NAFT). These techniques show a potential path towards an integrated fiber-coupled erbium single photon source.

1.1 Motivation

Quantum technologies are being looked to by many as one part of the solution for the rapidly growing global need for faster, more secure, and more specialized computing and communication [1]. At the basis of these quantum technologies, to make them useful and feasible for widespread adoption, there is a need to communicate quantum information between devices [2]. This can be done by transmitting quantum light, using spin states encoded in photons emitted by a single photon source [3], [4]. While there are many candidates for this and the field is growing quickly, an ideal single photon source is yet to be found [5].

The discovery of a high-quality single photon source that can be manufactured at scale for low-cost and easily integrated into devices would be disruptive for

the field of quantum technologies [6]. Single photon sources have been a major topic of study recently, but they remain expensive and unreliable to manufacture. Making single photon sources with high-quality characteristics such as low-loss transmission over optical fibers and long quantum coherence times would make research into quantum communication much more accessible, opening the door for a new era in quantum information science [5].

In this thesis, optical trapping is used to explore the optical properties of erbium-doped nanocrystals as a candidate for single photon sources and methods for producing integrated devices are developed. Erbium-doped nanocrystals can be pumped with low-cost lasers and exhibit luminescence at low-loss telecommunication wavelengths, ideal for transmission over fiber optic links [7]. Sources of single photons required a single nanocrystal containing a single active erbium emitter to be isolated [8].

Optical trapping is used to evaluate their feasibility as quantum light sources as it allows single particles to be isolated. Metallic nanostructures can be used with optical trapping to enhance the incident field and increase the optical forces, allowing evaluation of particles under 100 nm [9]. To measure the optical properties of single erbium-doped nanocrystals, they are optically trapped and excited using plasmon-enhanced double nanohole apertures. These nanostructures can also enhance the brightness of the light emitted by the erbium-doped nanocrystals, overcoming the low brightness typical of erbium emitters [10], [11]. With this enhanced brightness we are able to observe discrete levels of emission from the erbium-doped nanocrystals that correspond to the number of active erbium emitters present, which allows us to select nanocrystals with single active erbium emitters.

A photochemical method to permanently anchor nanocrystals inside of a DNH aperture while optically trapped was also explored. Emission enhancement and

isolation of erbium-doped nanocrystals can be applied in combination with the photochemical method and has the potential to yield a method to permanently anchor nanocrystals with single active emitters in place. This device could be used for quantum control at cryogenic temperatures, allowing for on-demand single photon production which can be coupled to an optical fiber for quantum communication. A potential candidate for direct fiber-coupling was also explored where a metallic aperture was fabricated on the tip of an optical fiber which was successfully used for optical trapping. Going further, the optical trapping and anchoring could be performed with an aperture on the tip of an optical fiber with the ultimate goal of producing a fully integrated fiber-coupled single photon source for manufacturing at scale.

1.2 Thesis Contributions

This thesis discusses novel methods based on optical trapping to use erbium-doped nanocrystals for quantum light sources. Four experiments demonstrate a route to a low-loss fiber-coupled single photon source:

1. The geometry of double nanohole apertures was tuned to maximize the emission from optically trapped erbium-doped nanocrystals.

2. Nanocrystals with single active erbium emitters were isolated using optical trapping with double nanohole apertures.

3. A novel method to selectively anchor nanoparticles within a double nanohole aperture during optical trapping was explored.

4. A low-cost fabrication method for integrated fiber optic nanoaperture tweezers was developed.

The author has contributed to one published work that is discussed in this thesis. The contributions of the individual authors are listed in the following section.

1.2.1 Isolating and Enhancing Single-photon Emitters for 1550 nm Quantum Light Sources Using Double Nanohole Optical Tweezers [12]

This work focused on using DNH optical tweezers to isolate dilutely erbium-doped nanocrystals and measure their emission to find nanocrystals with single erbium ions. This work builds upon previous work in our group by Alizedehkaledhi et al. which used rectangular apertures [10], [13]. This new study showed that the DNH structures significantly enhanced the emission, allowing for nanocrystals with single erbium ions to be detected much more quickly.

The experiment was designed by Zohreh Sharifi and Reuven Gordon. The experiments were carried out by Zohreh Sharifi and Michael Dobinson. Ghazal Hajisalem assisted with the experimental setup. Mirali Seyed Shariatdoust performed the FDTD simulations. Adriaan Frencken and Frank C.J.M. van Veggel synthesized the nanocrystals. The manuscript was primarily written by Michael Dobinson, with contributions from all other authors. The experiments described in sections 4.1 and 4.2 were based on this work.

1.3 Outline

This section gives an outline of the thesis chapters with a short description of their contents.

Chapter 1 introduces the topics of this thesis and provides the motivation behind the experiments.

Chapter 2 discusses the relevant previous work in the area of quantum light sources, optical trapping, and single emitter isolation.

Chapter 3 describes the experimental methods used and outlines the path towards an integrated fiber-coupled single photon source based on the four experiments.

Chapter 4 presents the experiments and discusses the experimental results.

Chapter 5 synthesizes the results of all experiments and compares them to other works.

Chapter 6 concludes the thesis and describes possibilities for future work.

Chapter 2

Theory and Prior Work

Single photon sources have been a major topic of research for many years but an accessible and low-cost high-quality source for manufacturing at scale is yet to be found [14], [15]. There are a wide range of candidates but single photon sources based on erbium ions are a leading candidate due erbium's emission at low-loss fiber optic telecommunication wavelengths and long coherence times. There are two challenges to be overcome with erbium emitters - their relatively low brightness (compared to other sources) and isolating single emitters with a reliable and scalable method [8], [13].

In this thesis we look at two approaches that can overcome these challenges. Metallic nanostructures such as the DNH are used to increase the brightness of erbium emitters by enhancing the emission rate through confinement of the source and enhancement of the local electric field with plasmonic resonances [16]. Optical trapping can also be combined with metallic nanostructures to isolate single emitter sources for evaluation. A photochemical method that is used with optical trapping to selectively and permanently anchor surface-modified single emitter nanoparticles inside of a nanostructure is also explored. A method for fabricating integrated nanoaperture optical fiber tweezers is also considered as emission from trapped particles can be directly coupled into the fiber. This chapter details the relevant prior work and theory in these areas.

2.1 Single Photon Sources

A device which is triggered to emit a single photon at a time is type of quantum emitter and is considered a single photon source. Single photon sources are unique as quantum information can be encoded in the emitted photon to make it a 'photonic qubit.' This information is typically encoded in the form of the polarization or energy of the photon [5]. Photonic qubits are a good choice for many quantum information science applications as they do not interact strongly with the environment, travel at the speed of light, and linear optical systems can be used to measure and manipulate them [5]. There is a wide range of candidates for single photon sources which include single emitters based on individual ions [8], [17], atoms [18], or molecules [19], [20], and other emitters based on solid-state technologies such as quantum dots [6], [21], colour centers [22], and atomic ensembles [23]. While there are many competing technologies, this section discusses single emitter sources; the advantages, disadvantages, and mechanisms of other types of single photon sources systems are outside of the scope of this thesis.

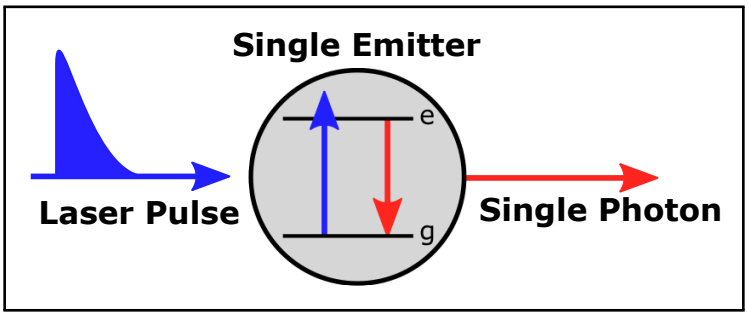

FIGURE 2.1: Illustration of a two-level single emitter which is excited by a laser pulse to produce a single photon. The transition from the ground state to the excited state caused by the laser pulse is shown in blue. The transition from the excited state to the ground state and the single photon emission are shown in red.

The specific mechanisms of single emitter systems can vary, but in general an optical or electronic signal causes the system to enter an excited state where a single

photon is emitted upon relaxation. Figure 2.1 shows a simplified schematic of a two-level single emitter system. In this schematic, a laser pulse excites the single emitter from the ground state, g, to the excited state, e. On radiative relaxation back to the ground state, a single photon is emitted. The radiative emission rate of the system is limited by the excited state lifetime and the relaxation time from the excited state back to the ground state [24].

Several applications in quantum computing, such as quantum teleportation protocols to send and receive quantum states, demand sources that can not only produce single photons but also require the initial and subsequent photons to be indistinguishable [2], [25]. Quantum cryptography protocols which use quantum key distribution demand single photons be sent securely over a channel as multiple photons encoded with the same quantum information could be measured by eavesdroppers to compromise the channel's security [26].

2.1.1 Characteristics of Single Photon Sources

A single photon source can be evaluated on a wide range of metrics, the following sections describe some of the most important characteristics and how they are measured.

Determinism

A deterministic source is capable of emitting a single photon on-demand, each input pulse produces a single photon. The determinism of a single photon source can be evaluated as the quantum efficiency, η, calculated by the ratio of the number of output photons, N_0, to the number of input pulses, N_i:

$$\eta = \frac{N_0}{N_i} \tag{2.1}$$

Consistency

The consistency of a single photon source is evaluated based on the probability of single photon emission. An ideal single photon source is consistent with a 100% probability of single photon emission and 0% probability of multiple photon emission. The consistency can be evaluated by measuring the degree of second-order coherence using Hanbury-Brown-Twiss (HBT) interferometry which directs the light source through a beamsplitter to two photodetectors [27]. This experiment allows the probability of detecting multiple photons to be measured as a true single photon source will never activate both photodetectors at the same time. The resulting metric is the $g^{(2)}(0)$ which is zero for an ideal single photon source. This metric is calculated using the observed time averaged photon number, $n(t)$, for a varying time offset, τ:

$$g^{(2)}(\tau) = \frac{\langle n(t)n(t+\tau)\rangle}{\langle n(t)\rangle^2} \tag{2.2}$$

Indistinguishability

In an ideal single photon source, the initial and subsequent photons are identical in every way. The property of indistinguishability can be measured by the visibility of the two-photon interference, known as the Hong-Ou-Mandel (HOM) effect [28]. This measurement is performed with interferometry. One approach uses a Mach-Zehnder interferometer, where the light source is directed through a polarizing beamsplitter, interfering the transmitted signal with a time-delayed version of the reflected signal, and then detecting the coincidence counts with two photodetectors [6]. Indistinguishable photons will both be directed to the same detector and the coincidence rate will be zero for no time delay with an ideal single photon source.

The visibility of the HOM interference, $\mathcal{V}$, is measured in this approach by rotating the polarization of the reflected signal to be parallel or perpendicular to the transmitted signal, then measuring the area under the $g^{(2)}(\tau)$ curve for τ near zero for each case, $A_{\parallel}$ and $A_{\perp}$, with zero time delay [6]. For measuring practical sources, corrections can be needed to account for a finite $g^{(2)}(0)$ [6]. The visibility is calculated simply by the maximum and minimum coincidence counts, $\mathcal{C}_{\text{max}}$ and $\mathcal{C}_{\text{min}}$, or by the parallel and perpendicular measurements mentioned previously:

$$\mathcal{V} = \frac{\mathcal{C}_{\text{max}} - \mathcal{C}_{\text{min}}}{\mathcal{C}_{\text{max}}} = \frac{A_{\perp} - A_{\parallel}}{A_{\perp}} \tag{2.3}$$

Repetition Rate

The repetition rate of a single photon source is determined by the maximum rate at which input pulses can be applied to produce single photons. For an ideal single photon source, this rate is arbitrarily fast, limited only by the duration of the single photon output pulses [5]. Practical sources are limited by their radiative emission rate and quantum efficiency. The input signal rate must be maintained at less than the maximum repetition rate of the single photon source.

Loss

Loss can occur in the coupling to a channel, as well as over the channel itself, and is and important parameter to be minimized for single photon sources. An ideal single photon source coupled to an ideal channel has zero coupling and zero channel losses. For practical sources and channels, one of the most common optical channels today is the single-mode optical fiber which is widely used in telecommunications for classical communication. The highest performance optical fiber

links have losses as low as 0.14 dB/km and operate in the infrared C-band, 1530–1565 nm [29]. The channel loss is calculated for a specific distance, l, for a channel with an attenuation factor at a specific wavelength, $\alpha_c(\lambda)$:

$$L_{\text{channel}} = \alpha_c(\lambda) l \tag{2.4}$$

The coupling losses can also be considered alongside the channel losses. These losses depend on the emission characteristics of the source and the specific channel properties. The total loss is calculated in units of dB using the ratio of the sent from the source and the photons received at the other side of the channel, N_0 and N_f:

$$L_{\text{total}} = 10 \log_{10} \left(\frac{N_f}{N_0} \right) = L_{\text{coupling}} + L_{\text{channel}} \tag{2.5}$$

2.2 Erbium as a Low-loss Single Photon Source

There are several rare-earth ions, including Pr^{3+}, Ce^{3+}, and Er^{3+}, that are good candidates for single photon sources as they exhibit stable emission and allow quantum state control [30]–[33]. Minimizing channel losses over optical fibers is a key motivation for finding a rare-earth ion based single photon source that operates in the low-loss infrared C-band, 1530–1565 nm. It is convenient then that the basic component of the widely used erbium-doped fiber amplifier (EDFA), the erbium ion, produces emission in the C-band and maintains high quality characteristics for quantum control [34]–[36]. To create a single photon source, a single erbium ion is embedded in a larger host crystal which can be physically manipulated and coupled to a channel. The single erbium emitter can optically excited with laser pulses to emit photons in the range of 1530-1565 nm [36]. These properties of erbium ions

make them a good candidate for single-photon sources for quantum communication over fiber, however the characteristics of specific erbium-based single emitter devices must be evaluated individually.

Erbium's optical properties have been of interest for many years in telecommunications applications, with the 1.5 µm transition being widely used in EDFAs for long-distance optical fiber links [7]. The spectroscopic properties of the erbium ion and erbium-doped materials have been explored in-depth, with well-studied optical transitions, linewidths, and dephasing times [35], [36].

Figure 2.2a shows several common optical transitions of erbium, including ground state (dashed lines) and excited state (dotted lines) absorption transitions, several visible and NIR radiative transitions (solid lines), and intermediate phonon relaxation (curly lines). The energy levels are denoted by the atomic term symbols in the form $^{2S+1}L_J$, where S is the spin quantum number, L is the orbital quantum number, and J is the angular momentum quantum number [36]. Erbium materials have limited brightness due to long excited state lifetimes, on the order of 10 ms for most host crystals which limits the photon emission rate [36]. These materials also exhibit narrow linewidths in high magnetic fields, as narrow as 78 Hz at 5 T in dilutely-doped Y_2SiO_5 at 2 K [36]. This narrow linewidth gives significant margin for emission rate enhancement which can increase the brightness, typically at the expense of linewidth [37].

Figure 2.2b shows the electronic structure of an erbium ion in a host crystal. The electronic crystal field causes Stark splitting of the energy levels of the Er^{3+} ion by Kramer's theorem into J + 1/2 doublets, i.e. 8 states for the $^4I_{15/2}$ level and 7 states for the $^4I_{13/2}$ level [7]. These doublet states are further separated through Zeeman splitting where an external magnetic field affects the energy difference between the split spin-up and spin-down states for an electron in that energy level. This changes the energy of the electron the emitted photon which corresponds to

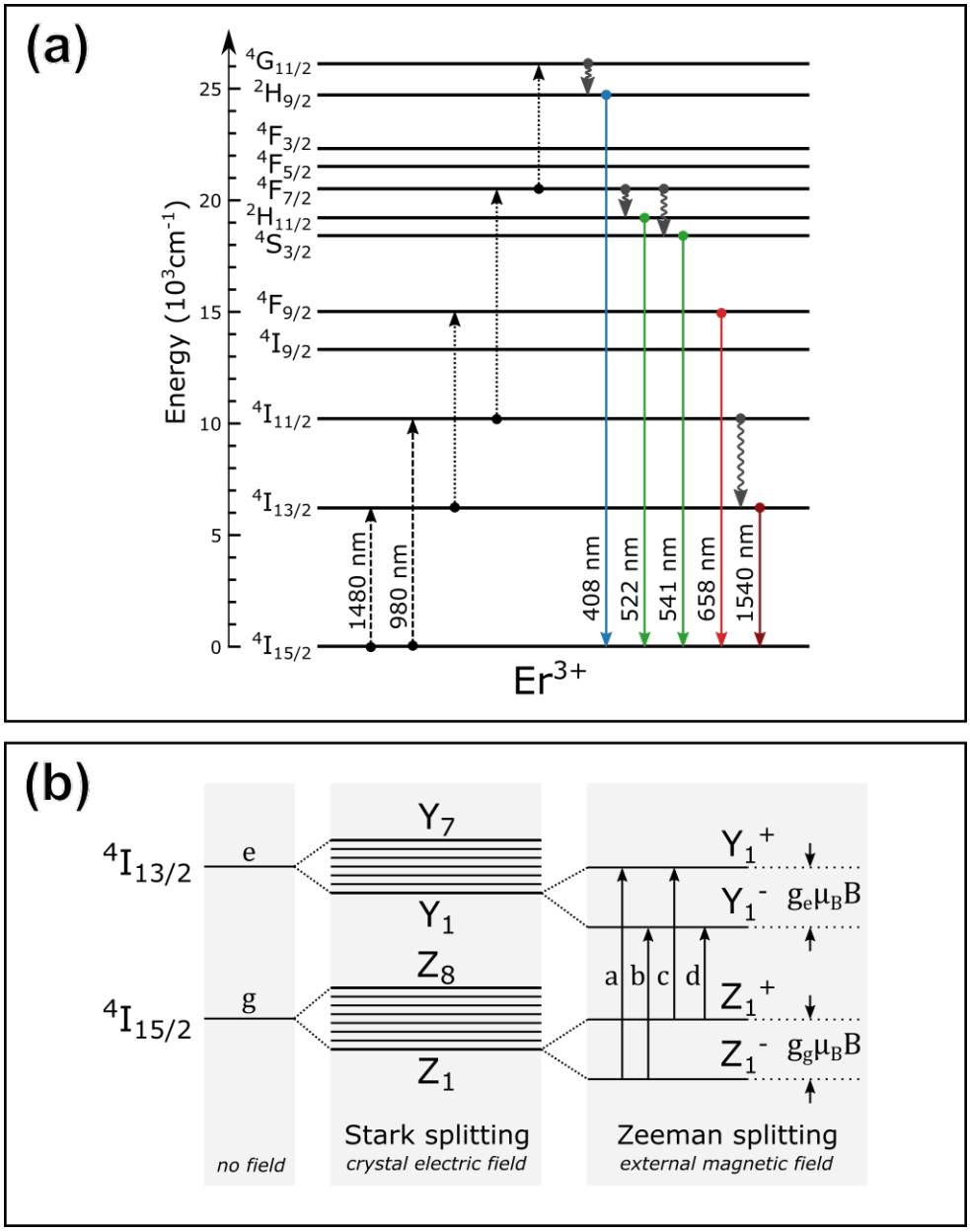

FIGURE 2.2: Erbium energy diagrams. (a) Optical transition diagram showing absorption transitions (black solid lines), radiative transitions (coloured solid lines), excited state absorption (dashed lines), and multiphonon relaxation (curly lines) (Adapted from Suyver et al. [11]) (b) Optical transitions of Erbium within a magnetic field. The $^4I_{15/2}$ is split into 8 Kramer's doublets, Z_1 to Z_8, and the $^4I_{13/2}$ is split into 7 doublets, Y_1 to Y_7. Each doublet is shown split into two further states corresponding to spin up, $+$, and spin down, $-$. Adapted from Bottger et al. [35].

the spin state of the excited electron; this is detectable by small shift in the wavelength of the photon [8]. For practical applications, low temperatures can be used to maintain the lowest energy state in the Stark manifold to excite the transitions shown in figure 2.2b [38].

Erbium has been shown to be a good candidate for quantum communication as its quantum state can be controlled through coherent spin and optical transitions [34], [35]. This persists even when embedded in a solid-state host crystal as the active $4f$ electrons are shielded by the $5s$ and $5p$ electrons which reduces external phonon coupling [36].

2.3 Emission Rate Effects on Quantum Emitters

When a quantum emitter such as a fluorescent nanoparticle is optically confined, its emission is influenced by the confinement. This can lead to an increase in the spontaneous emission rate of the particle due to the high density of optical states within the small volume as the reflected field interacts with the emitter, referred to as the Purcell effect [24], [38]. The confinement can also lead to a reduction in the emission rate when too close to the interface due to phonon coupling, referred to as fluorescence quenching [24].

Figure 2.3 shows a three-level quantum emitter system. State 1 is the ground state from which it is excited to state 2, a virtual state. This state relaxes to state 3 with the energy released at the rate, γ_{relax}. The system can then decay from state 3 to state 1 either radiatively or non-radiatively, with the total decay rate being a combination of the radiative and non-radiative decay rates, γ_r and γ_{nr}.

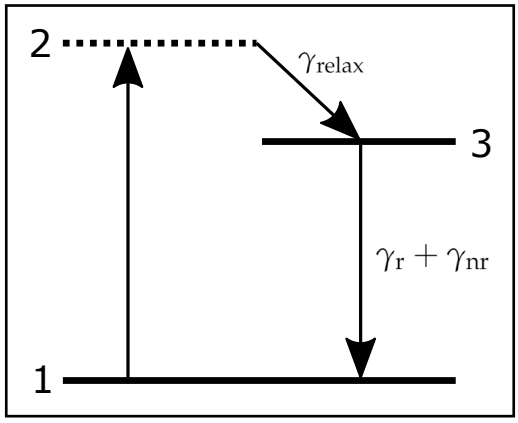

FIGURE 2.3: Three-level quantum system with a virtual state. Relaxation from state 2 to state 3 occurs at the rate γ_{relax}. Relaxation from state 3 to state 1 can occur radiatively or non-radiatively at the rates γ_r and γ_{nr}.

2.3.1 Quantum Rate Enhancement

Emission occurs by radiative relaxation in a quantum emitter system, which is limited by the radiative decay rate, γ_r. However, the system can also relax non-radiatively by phonon vibrations, heat, and other unwanted coupling [24]. The surroundings of a quantum emitter can affect both the radiative and non-radiative emission rates [39], [40]. If the radiative rate is enhanced, the overall emission rate increases, whereas if the non-radiative rate increases, the emission is quenched. The overall quantum efficiency of the system, η_0, is calculated by the following [24]:

$$\eta_0 = \frac{\gamma_r}{\gamma_r + \gamma_{\text{nr}}} \tag{2.6}$$

Simple resonant cavities can be designed to confine a quantum emitter to increase the spontaneous emission rate by the Purcell effect, this is also known as quantum rate enhancement. The Purcell factor, F_P, is equivalent to the magnitude enhancement of the emission rate, γ/γ_0. For a simple resonant cavity it is calculated using the quality factor, Q, and mode volume, V, of the cavity:

$$F_P = \frac{\gamma}{\gamma_0} = \frac{3}{4\pi^2}\left(\frac{\lambda}{n}\right)^3\left(\frac{Q}{V}\right) \tag{2.7}$$

Metallic nanostructures can be designed to both confine the quantum emitter and use plasmonic effects to enhance the local electric field [24]. Plasmonic enhancement from the nanostructures can concentrate the field which can increase absorption and affect both the radiative and non-radiative decay rates [39]–[42]. This increased local field in turn increases the relaxation rates according to Fermi's golden rule [24].

2.3.2 Fluorescence Quenching

A fluorescent particle can transfer excitation energy to its surroundings in many non-radiative forms including phonon coupling [24]. This occurs due to the difference in the electronic states of the system and its surroundings, such as when a quantum emitter particle is embedded in a solid, in a liquid medium, or near an interface [24]. This may be significant when the emitters are embedded near the surface of a particle, such as in lanthanide-doped nanocrystals [43], [44]. All of these cases can cause a reduction in the the quantum efficiency, as the excitation energy is converted and absorbed by the surroundings rather than emitting a photon [24].

Figure 2.4 shows an example of a system in which a light pulse excites a particle which is strongly coupled to its surroundings. In this case, the light pulse is converted to a phonon and the energy is transferred to the surrounding environment, rather than resulting in radiative relaxation. When near an interface or in a strongly coupled system, heat, surface modes, and unwanted waveguide modes can also couple energy away from radiative pathways, resulting in fluorescence quenching [24].

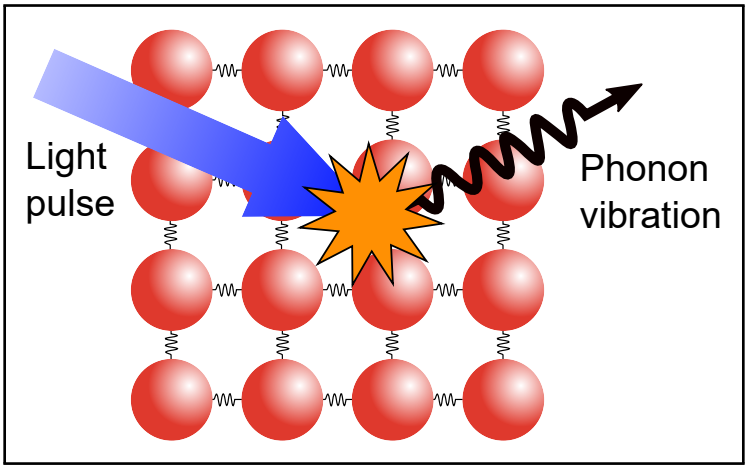

FIGURE 2.4: Illustration of a phonon vibration excited by a light pulse that couples into the rest of the system. The example system consists of mechanically linked particles, similar to a crystal structure.

Fluorescence quenching is typically a negative effect for nanoparticles that are quantum emitters as the emission is significantly reduced when the particle is near an interface or embedded in media. With a uniform distribution of active emitters in the small volume such as a nanoparticle, a significant proportion of the active emitters which are near enough to the surface can couple to their surroundings and become quenched. This can be minimized with careful preparation of the nanoparticles using a passive shell to cover the active region [43].

2.3.3 Phonon Relaxation Rates

Phonon scattering in a system is limited to a specific rate, depicted as a relaxation rate, γ_{relax}, from the virtual state shown in figure 2.3. It should be noted that quantum rate enhancement by confinement does not necessarily affect the phonon relaxation rates in the same way as the absorption and radiative rates. The virtual state lifetime can become the limiting factor when the other rates are maximized. The erbium ion system shown in figure 2.2a must undergo a non-radiative transition from the ${}^4I_{11/2}$ level to the ${}^4I_{13/2}$ when excited with 980 nm light, before it

can radiatively decay back to the ground state [7]. This excited state lifetime is on the order of microseconds and has the potential to limit the repetition rate of an erbium-based single photon source to the kilohertz regime [7]. To overcome this, the system can instead be excited with 1480 nm light which can excite the system to a virtual state with slightly higher energy than the ${}^4I_{13/2}$ energy level [7]. The lifetime of this virtual state can be significantly shorter, on the order of 10's of nanoseconds [7]. This nonradiative relaxation rate, A_{NR}^{-}, is calculated for a single phonon in an erbium doped host crystal using the following equations [7]:

$$A_{NR}^{-}(T) = B[n(T) + 1]e^{-\beta \Delta E} \tag{2.8}$$

where B is a constant dependent on the host material, $\beta = -\log(\varepsilon)/\hbar\omega$, ΔE is the energy gap, and $n(T)$ is the Bose-Einstein occupation number of the phonon mode [7]:

$$n(T) = \left(e^{\frac{\hbar\omega}{k_B T}} - 1\right)^{-1} \tag{2.9}$$

As values for B and β have not been reported for $NaYF_4$, a similar crystal, $LiYF_4$, has been used in literature as a close approximation, i.e., $B = 6.4 \times 10^7$ s^{-1} and $\beta = 3.6 \times 10^{-3}$ cm [45]. In this case, the single phonon relaxation rate was calculated to range from $(4.0\text{–}8.5\text{ ns})^{-1}$, for a typical energy gap between 50-100 cm^{-1}. It is clear from this calculation that if the ${}^4I_{11/2}$ relaxation rate is limiting emission, it may be favorable to excite to a lower energy virtual state to exploit the faster phonon decay.

2.4 Isolating Single Emitters

Single emitters are good candidates for single photon sources, and erbium emitters have particularly promising properties, but a scalable method to isolate single

emitters which reliably produce emission is still a topic of research [14]. A variety of techniques have been explored to isolate a wide range of single emitter candidates such as lanthanide ions [30], [37], [46], artificial atoms in silicon [22], and quantum dots [6], [21], [47], but all current methods rely on either searching in a random distribution, or ion implantation.

Methods that search random distributions of emitters require significant post-processing time to find and couple to the single emitters as they must be differentiated from multiple emitters and devices that do not emit [22]. This issue also exists with emitters embedded within devices such as photonic crystals, as each device must be probed to determine if a single emitter is appropriately coupled to the device after fabrication [37]. Ion implantation shows high accuracy for implanting single emitters into photonic integrated circuits, but the implanted ions are not always active [46]. This has been demonstrated for praseodymium ions with a reported yield of 50% [46].

Our group has recently demonstrated a new method that allows for active single emitter sources to be found and isolated in real-time, rather than post-processing the distribution. This method was developed by Alizadehkhaledi et al. in 2020 using erbium-doped $NaYF_4$ nanocrystals with nanoaperture optical trapping to both enhance the erbium emission and isolate the nanocrystals with single active emitters [10], [13]. In this method, the erbium-doped nanocrystals are optically trapped in a rectangular aperture and the emission of the isolated emitters is measured in real-time to determine if the trapped nanocrystal has a single active emitter.

2.5 Optical Tweezers

Optical tweezers use optical forces to hold particles in space, typically using a focused laser. Conventional optical tweezers employ a single focused beam and are

effective for dielectric particles in the Rayleigh and Mie regimes that are larger than ~100 nm without requiring excessive optical powers that can damage the particles [48]. Nanoaperture optical tweezers can probe much smaller particles with low optical powers, allowing single proteins in the single nanometer range to be trapped without damage [49], [50]. Despite the wide range of applications for nanoaperture optical tweezers, their adoption remains limited partly due to the complicated optical setup and nanofabrication requirements [51]. Integration of a nanoaperture on an optical fiber can lower the barrier of entry for nanoaperture optical trapping, as it eliminates the need for nanofabrication and optical alignment for the end-user. Methods to fabricate these nanoaperture fiber tweezers have been demonstrated using focused-ion beam milling on the fiber face [52] and template-stripping [53].

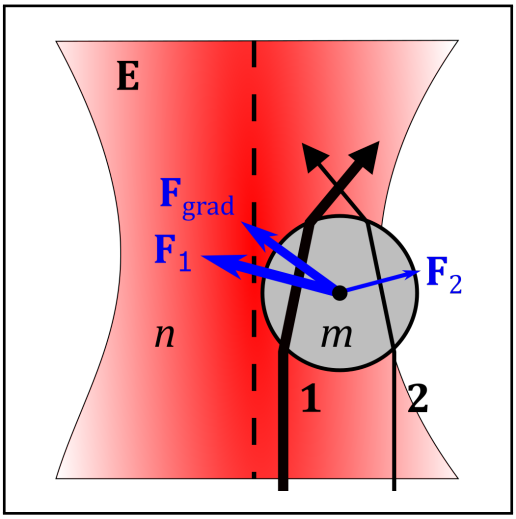

FIGURE 2.5: Ray optics illustration of optical trapping. The beam intensity, **E**, is maximum in the middle of the beam waist in a medium with refractive index n. The force exerted on the particle, with refractive index m, by rays 1 and 2 are labeled $\mathbf{F}_1$ and $\mathbf{F}_2$. The resulting gradient force is labeled $\mathbf{F}_{\text{grad}}$ which moves the particle into the center of the beam.

2.5.1 Single-Beam Optical Tweezers

Optical trapping exploits the the gradient force exerted by a focused laser on a particle which has a different refractive index than the surrounding media. The utility of this effect was first discovered by Ashkin et al. in 1986 and has since expanded to become a widely used technique for holding and manipulating nanoparticles [48]. The focused beam exerts a gradient force F_{grad}, which is a restoring force that maintains the particle in the most intense region of the field.

Figure 2.5 shows, from a ray optics approach, how the refraction from rays of light entering the particle exert forces on the particle due to a change in the direction of their momentum vector. The gradient force restores the particle to the position of highest intensity and is balanced against the scattering force to hold the particle in an optical trap. However, this ray optics approach only holds for particles in the Mie regime that are larger than the wavelength of the incident light [48].

Smaller particles in the Rayleigh regime, $2r < 0.2\lambda$, can be trapped with a single focused beam, but the intensities required are very large and can cause significant heating and damage [48]. This is due to Rayleigh scattering which exerts a force in the direction of the incident power which scales proportional to r^6 [48]. This scattering force must be balanced with the gradient force to keep the particle trapped, which is challenging for smaller particles as the gradient force scales proportional to r^3 [48]. In this regime the gradient force depends on the electric field gradient $\nabla \mathbf{E}$, the refractive index of the medium n_m and the particle n_p, where the effective index of the particle $m = n_p / n_m$ [48]:

$$\mathbf{F}_{\text{grad}} = \frac{n_m^3 r^3}{2} \left(\frac{m^2 - 1}{m^2 - 2} \right) \nabla \mathbf{E}^2 \tag{2.10}$$

2.5.2 Nanoaperture Optical Tweezers

Nanoapertures and other metallic nanostructures have been investigated for improving optical tweezers for decades as they exert radiation forces and have significant effects on the local electric field [54]–[56]. A variety of structures have been proposed such as metal tips [57], patterned surfaces [58]–[60], and nanoapertures [9], [61]. Nanoapertures in particular are of interest to the field of optical trapping as they have been shown to improve the trap stiffness through an effect known as 'self-induced back-action' (SIBA), which uses a nanoaperture to enhance the local electric field while the particle being trapped influences the optical transmission to maintain the trap [49].

The theory of SIBA was described and experimentally confirmed by Juan et al. in 2009, showing that particles under 100 nm could be trapped with low laser power [49]. This work builds upon the 1999 theory of Okamoto and Kawata which showed that a particle near a nanoaperture is drawn towards the aperture from the radiation force, and that this force can overcome gravity and thermal forces [54]. SIBA also relies on the influence of the dielectric particle on the transmission through the aperture. When a particle with a higher refractive index than the surrounding media enters the subwavelength aperture, the change in the refractive index of the aperture increases the transmission through the aperture according to Bethe's aperture theory [62]:

$$T \propto \left(\frac{nr}{\lambda}\right)^4 \tag{2.11}$$

This change in transmission corresponds to a change in the photon flux, and thus photon momentum, through the aperture. If the trapped particle attempts to exit the aperture, due scattering or thermal forces, the effective size of the aperture and transmission decreases, increasing the optical forces on the particle, restoring

it back into the aperture. This momentum balance results in the particle becoming optically trapped within the aperture. A variety of different apertures have been investigated in past works including rectangular [63], double nanohole (DNH) [64]–[67], and bowtie apertures [68]–[70].

Apertures in metal films also exhibit plasmonic resonances which can be tuned by changing the shape of the aperture and can enhance the local electric field within the aperture [71]. This can provide a stronger restoring force for stiffer trapping and, for fluorescent particles, can increase the excitation energy intensity [64], [71]. Nanostructures can also be designed to have multiple plasmonic resonances [10], [71], [72]. Optical tweezers have also been adapted to benefit from thermophoretic forces [73], [74] and nanopore technologies [75]–[77] which can aid in bringing particles to the region of interest.

Nanoaperture trapping is particularily appealing for biological studies as it enables label-free study of biomolecules, can be performed in heterogenous solutions, and may be used to study conformational changes of proteins [78]–[80]. The binding dynamics of single molecules to single proteins can also be probed with nanoaperture trapping, a feature that is of great interest for drug discovery [81]–[83].

2.5.3 Fiber-based Nanoaperture Optical Tweezers

Optical fibers with tapered tips can be used directly in solution to optically trap large particles and nanoapertures patterned on the tip of optical fibers allow for trapping much smaller nanoparticles [84]. A major challenge with nanoaperture optical trapping is the experience needed to build and align an optical trapping setup, as well as need for nanofabrication facilities and experience [51]. Optical trapping of single proteins and other biomolecules is a promising area that has not

yet fully embraced nanoaperture optical trapping and could benefit greatly from more accessible fiber-based devices [51].

Developing an accessible device which integrates a nanoaperture on the tip of an optical fiber would allow the end-user to use a simple setup contained entirely in fiber which requires minimal optics and nanofabrication experience, expanding the technique to many more researchers. Several methods have been explored for fabricating optical fibers with nanoaperture tips using focused-ion beam milling on the tip of the fiber [52], [69] and template stripping [53], [85]. However, these fabrication methods rely on expensive top-down manufacturing techniques such as focused-ion beam milling and scanning electron microscopy which limits their accessibility.

Optical trapping with nanoaperture optical fiber tweezers operates on a principle similar to SIBA and is performed by exciting the structure with a laser coupled directly to the fiber. The transmission through the aperture and the reflection from the fiber face are both signals that can be measured to detect trapping and monitor the dynamics of the trapped nanoparticles [53], [69]. Another major advantage of integrating the nanoaperture on the tip of an optical fiber is that the emission from a trapped fluorescent nanoparticle can be coupled into the optical fiber [85]. This coupling is typically weak for subwavelength particles due to broad scattering [49], but it has been shown that the coupling may be improved by integrating a grating [85].

2.6 Nanoparticle Anchoring with Chemical Methods

A method to anchor nanoparticles to a gold nanostructure was explored in this thesis which uses two chemical reactions: gold-thiol bonding and photochemical protection. Gold-thiol bonding is the reaction that is responsible for thiol groups

attaching to gold surfaces. Photochemical protection has many applications and is used to protect part of a larger molecule until triggered by light.

2.6.1 Gold-Thiol Bonding

The strong affinity of sulfur with gold causes a bond to be formed between thiol (-SH) end-groups and gold surfaces [86]. Figure 2.6 shows this reaction in which the molecule of interest has a thiol (-SH) end group which is adsorbed onto the gold surface. The thiol group first forms a weak bond through physisorption before the S-H bond is broken through chemisorption to form an Au-S bond [87]. This reaction is applied to anchor nanoparticles by modifying the surface of the nanoparticles to add thiol end-groups. This reaction is used widely in nanofabrication to create self-assembled monolayers (SAMs) of organic molecules [86].

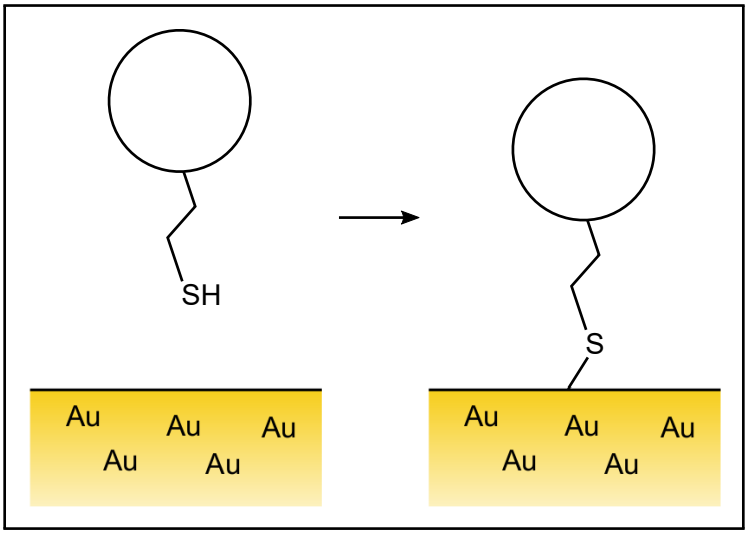

FIGURE 2.6: Illustration of a thiol end group on a larger particle bonding to the Au surface. This forms a sulphur bond that connects the two.

2.6.2 Photochemical Protection

Photoremovable groups are used to protect groups on a molecule until a photochemical reaction is triggered [88]. Ultraviolet light is a common trigger used in many types photochemical reactions due to its high photon energy which is easily absorbed [88]. A specific photochemical reaction is of interest in this thesis, the reaction of a photoremovable protecting group 2-bromo-4'-hydroxyacetophenone which is bonded to nanoparticles coated with a DSPE-PEG-SH layer which is used in the experiment presented in section 4.3. As the precise bonding of the group to the nanoparticle surface has not yet been confirmed for our experiments, the known reactions of one of the likely resulting groups, *p*-hydroxyphenacyl (pHP) will be discussed.

Applications of photochemical protection cover a wide range of biological and other applications and *p*-hydroxyphenacyl is of particular interest due its rapid release rate [88]. This group has enabled biological applications such as rapid phototriggered release of bioactive phosphates [89] and for protection of peptides for rapid activation of biological receptors [90]. Similar photochemical methods have also been used in UV-triggered thiol-yne 'click' reactions in which a photochemical reaction triggers bonding between surface-modified particles and the surface-modified substrate [91].

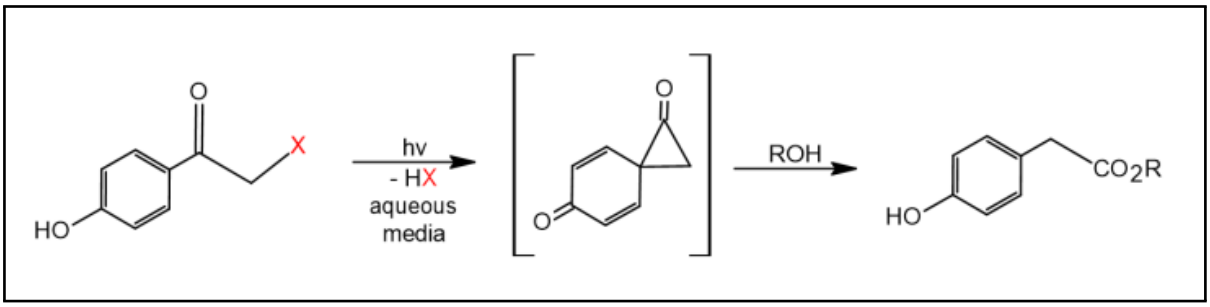

FIGURE 2.7: Photochemical reaction of *p*-hydroxyphenacyl (pHP) in aqueous media with the intermediate shown. Adapted from Klán et al. [88]

Figure 2.7 shows the general reaction of *p*-hydroxyphenacyl, with the intermediate step shown [88]. In this reaction, the photoremovable group is bonded to a larger molecule through the atom marked with the red X which can be a reactive group such as a thiol. This is what the photoremovable group protects, as without it the end-group of the larger molecule can react. When UV light is applied, the photoremovable group detaches to become inert in the solution. The molecule can then react using the now-exposed group. If the protected reactive group is a sulphur atom, de-protection allows the larger molecule to bond to gold through the exposed thiol.

Chapter 3

Methods

The experiments presented in this thesis use optical trapping methods with nanofabricated structures to evaluate the properties of erbium-doped nanocrystals. A photochemical method to anchor the nanoparticles and a method to fabricate the structures at the end of an optical fiber are also investigated. The following sections detail the goals of the experiments and describe the experimental methods used for optical trapping and spectroscopy, as well as the sample preparation and nanofabricaton methods.

3.1 A Path to an Integrated Fiber-Coupled Single Photon Source

In this thesis, four experiments depict a route towards using erbium-doped nanocrystals as single photon sources through optical trapping methods. These experiments as well as as their goals are listed below:

Optimizing DNH Geometry Maximize the brightness of trapped erbium-doped nanoparticles by tuning the DNH aperture geometry.

Observing Discrete Emission Observe discrete emission levels dilutely erbium-doped nanoparticles optically trapped in double nanohole apertures.

Anchoring Nanoparticles Explore a photochemical method to selectively anchor trapped nanoparticles in the DNH aperture.

Fabricating Nanoaperture Fiber Tweezers Develop a low-cost method to fabricate optical fibers with DNH apertures at the tip for fiber-based trapping.

The combination of these methods have the potential to yield a fiber-coupled single photon source based on erbium-doped nanocrystals anchored in a double nanohole aperture.

3.2 Optical Trapping

Optical trapping is performed by a focused laser using the optical setup shown in figure 3.1a. The transmission through a nanoaperture is measured which indicates if a particle is trapped by a distinct jump in the transmission and a change in the variation of the signal. The size of the particle can be determined by the amplitude of this variation. Different particles yield different sized jumps and RMS variation amplitude, as well as different characteristic behaviour and time to trap [64]. The particle's behaviour when entering and while inside an optical trap is observed by these characteristics of the transmission and can be affected by the geometry and mass of the particle, as well as the solvent. Light scattered by the trapped particle can also be measured. To perform optical trapping, a sample is prepared containing the analyte in contact with DNH apertures. This section details sample encapsulation and the optical trapping processes.

3.2.1 Sample Encapsulation

A sample is prepared by encapsulating the analyte in a sealed well in contact with the double nanohole substrate. Samples are prepared by placing a 0.12 mm thick

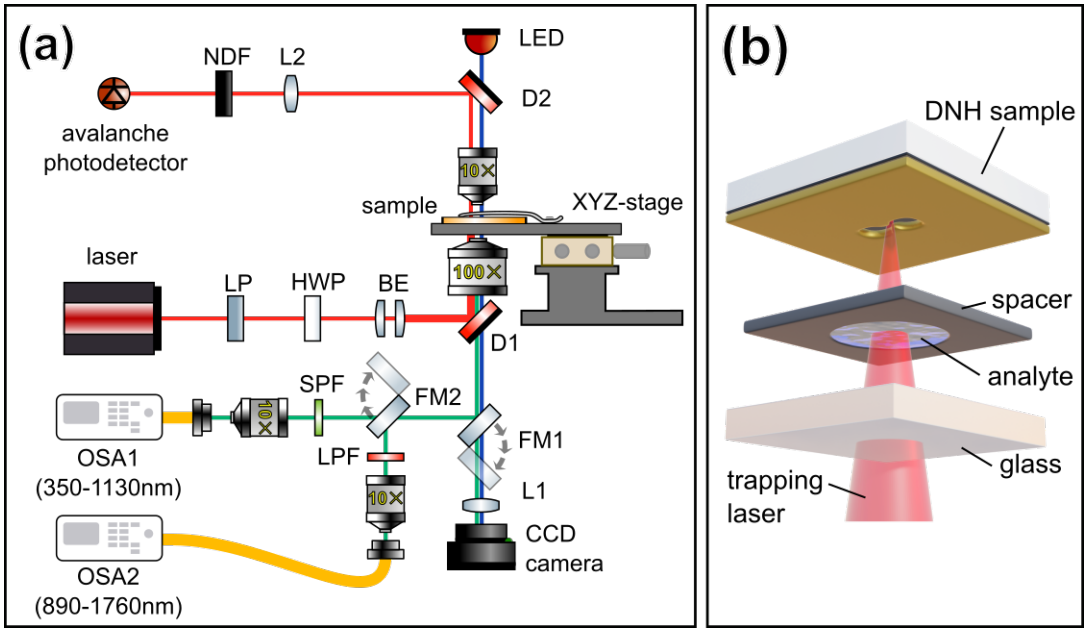

FIGURE 3.1: (a) Schematic of a typical optical trapping setup. (b) Exploded diagram of the encapsulated sample. The gold substrate is shown on the bottom with the adhesive spacer and analyte above. The gold DNH sample is shown at the top of the diagram. The trapping laser is shown focused on the DNH in red.

adhesive spacer (Grace Bio-labs, SecureSeal) on a glass coverslip. The analyte (typically 10 µL) is pipetted into the well and the gold double nanohole sample is placed in contact on top. This is placed in the optical trapping setup in the inverted configuration as shown in figure 3.1b.

3.2.2 Trapping

Optical trapping is observed by measuring the transmission of the laser through the aperture using an avalanche photodetector (APD). The change in the transmission level and the signal variation are key parameters to confirm trapping of a particle. This gives information about the size of the particle and can give insight into whether a particle undergoes a deformation in the trap, or if multiple particles are trapped [80].

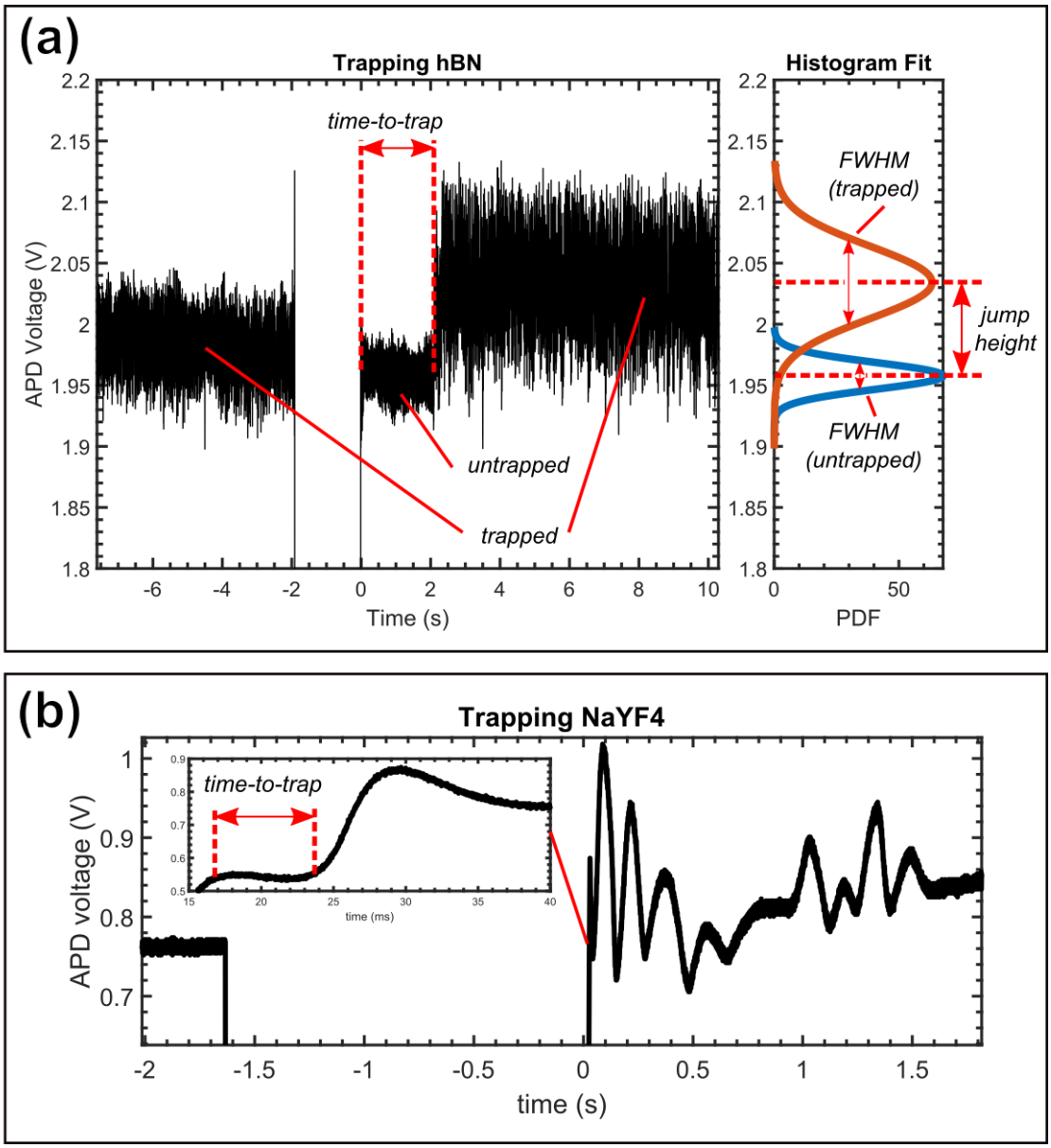

FIGURE 3.2: Trapping signal labeled with common parameters used to describe trapping. Signal is of the transmission, as measured by the APD, through a DNH during trapping of (a) hBN in water and (b) $NaYF_4$ nanocrystals in hexane.

Figure 3.2a shows a typical trapping signal in which a hexagonal boron nitride (hBN) particle is trapped in a DNH. The trapping signal shows the transmission through the DNH as measured by the APD. When trapping occurs, there is a distinct change in the level of transmission, the difference between the original transmission level and the final level is referred to as the *jump height*. The jump height can vary depending on the size and refractive index of the particle being trapped [9].

Figure 3.2b shows a trapping signal from $NaYF_4$ nanocrystals dispersed in hexane being trapped in a DNH. When trapping in non-polar solvents such as hexane, a large oscillation after turning on the laser is the indicator for trapping [10]. This oscillation is consistent for trapping in hexane but is not observed in water and is not caused by the monitoring circuit electronics. Hydrodynamic interactions combined with the trapping potential are a possible cause of this effect, but it has not been analyzed in detail.

Before a particle is trapped, the transmission signal has a particular noise distribution which can be measured by the variance of the signal. A histogram of the transmission signal can be fit with a Gaussian distribution and the full-width at half-maximum, *FWHM*, of this fit is also an indicator for trapping. When a particle is trapped, the movement of the particle causes the variation in the transmission signal to increase, causing a larger FWHM to be measured. This can be seen clearly in figure 3.2a. The character of the noise also gives information about the trapped particle and autocorrelation of the signal can give information about the size of the particle and its state [64]. Further investigation of the oscillations from trapping in non-polar solvents (figure 3.2b) is needed as they may also yield information about the trapped particle. Typically only a single particle is trapped at a time. In some rare cases, multiple particles can become trapped in an aperture. This can be trivially determined by the presence of multiple jumps in the transmission.

The time from when the laser excites the aperture to when a particle is trapped is referred to as the *time-to-trap* and can be seen in figure 3.2. This time is typically on the order of seconds for trapping in polar solvents such as water and milliseconds for non-polar solvents such as hexane. The substrate can also have an effect on this parameter as the surface charges of glass are much higher than for plastic which can repel particles and increase the time-to-trap [92]. Thermal effects can also play a role as the laser causes local heating of the DNH which can repel thermophobic particles. Surfactants such as sodium dodecyl sulfate (SDS) can be used to overcome the thermophoretic force to increase the trapping efficiency [73].

3.3 Spectroscopy

The optical setup used for trapping can also measure the light emitted by trapped nanoparticles. A spectrometer in the reflection path measures the power spectrum of the reflected light, with the incident laser light being removed with filters. Depending on the setup, either a bifurcated fiber or a flip mirror allows the visible and NIR spectra to be collected by two separate spectrometers. The visible spectrum is measured by an Ocean Optics QE65000 spectrometer, with a wavelength range of 350–1130 nm. The near-infrared spectrum is measured by a BaySpec NIRS-0900-1700, with a wavelength range from 890–1760 nm. Before measurements, the spectrometer is allowed to cool down for 30 minutes to ensure minimal thermal background noise.

3.4 Nanofabrication

The four different experiments required fabrication of DNH apertures and nanoparticles with a wide range of properties. The general nanofabrication processes are

detailed below and the specific DNH apertures and nanoparticles used in each experiment can be found in their relevant section.

3.4.1 Double Nanohole Apertures

A colloidal lithography method, used extensively by our group, was used to fabricate the DNH apertures used in the experiments [93]. This technique is fast and low-cost compared to traditional top-down methods that use focused ion beam (FIB) milling. In brief, monodisperse polystyrene nanospheres in ethanol are drop-coated on a glass substrate and allowed to evaporate. This forms a colloidal mask with a distribution of spheres on the surface of the substrate with single isolated spheres as well as larger planar structures with two or more spheres in direct contact with each other. This is followed by plasma etching which reduces the size of the deposited polystyrene spheres and allows the final aperture diameter and cusp separation to be tuned with precision [93]. Next, a 7 nm titanium adhesion layer followed by a 70 nm gold layer are typically sputtered onto the substrate using the Mantis QUBE sputtering system which has high film adhesion and surface uniformity [94]. If fabricating samples designed for colloidal pattern transfer, no titanium adhesion layer is used to facilitate removal of the gold layer.

After sputtering, the polystyrene spheres can be removed either by sonicating the sample in ethanol or using adhesive tape to remove the spheres [92]. Damage to the gold surface during removal of the polystyrene spheres is uncommon but can occur with excessive sonication or tape removal if the adhesion to the substrate is poor. This can be avoided by ensuring good adhesion with thorough cleaning of the substrate prior to fabrication and using sonication durations under 10 minutes. This results in a gold film with a variety of single, double, and clustered nanoholes.

Figure 3.3 shows an SEM image of a DNH produced using this colloidal lithography method. Different aperture diameters and cusp separations, labeled d and c, are achieved by tuning the plasma etching time [93]. The initial size of the polystyrene spheres can also be changed to vary the size of the apertures.

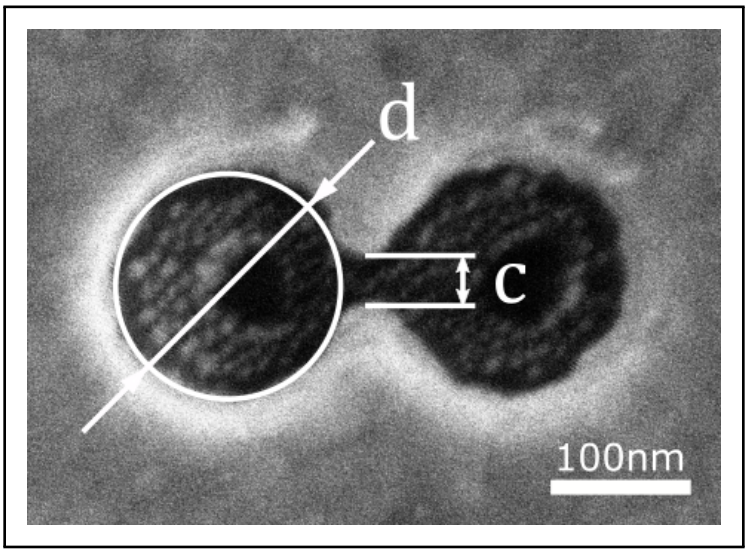

FIGURE 3.3: Image of a double nanohole taken with a scanning electron microscope (SEM), labeled with the critical dimensions. The aperture diameter, d, is the diameter of each nanohole. The cusp separation, c, is the distance between the two central cusps.

3.4.2 Nanoparticles

The main nanoparticles used in this thesis are $NaYF_4$ nanocrystals. These nanocrystals can be doped for upconversion with a Yb sensitizer and Er activator, or with Er alone. The surface can also be modified for dispersion in water and functionalized with photoprotected thiol groups. The $NaYF_4$ nanocrystals analyzed in this thesis were synthesized by Adriaan Frencken of Frank van Veggel's group.

The synthesis was based on previously reported work for lanthanide-doped hexagonal-phase $NaYF_4$ nanocrystals used for upconversion [95]. The properties of $NaYF_4$ as a host crystal have also previously been studied for a wide range

of lanthanide dopants including Tm, Er, Yb, and Eu [11], [45], [96], [97]. The $NaYF_4$ nanocrystal was chosen as the host-lattice allows highly efficient substitution of the yttrium with erbium and ytterbium dopants and has low energy phonon modes [11], [36].

Figure 3.4a shows a TEM image of a distribution of hexagonal $NaYF_4$ nanocrystals with a nominal diameter of 26.2 ± 2.7 nm. When designed for upconversion, the $NaYF_4$ nanocrystals are doped with 18% Yb and 2% Er. This allows for significant energy transfer upconversion to occur, allowing strong emission [11]. The nanocrystals can also be dilutely doped with low levels of erbium to investigate the properties of nanocrystals with discrete levels of emitters. The doping levels per nanocrystals are expected to follow a Poissonian distribution, with a uniform distribution expected within the nanocrystal volume. Both of these doped nanocrystals are dispersed in hexane for the work presented in this thesis.

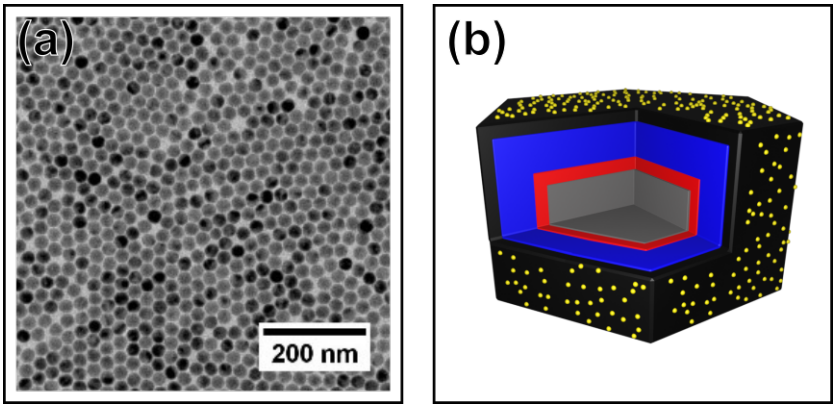

FIGURE 3.4: (a) TEM image of $NaYF_4$ nanocrystals with a nominal diameter of 26.2 ± 2.7 nm. (b) Cross-sectional diagram of a $NaYF_4$ nanocrystal (grey) coated with oleic acid (red) and DSPE-PEG (blue). The top layer of DSPE-PEG has methyl end-groups (black) and is functionalized with photoprotected thiol end-groups (yellow) in a ratio of 10:1.

Figure 3.4b shows a diagram of the photoprotected nanoparticles that were explored in the anchoring experiments. The surface of $NaYF_4$ nanocrystals can be modified for different applications. These photoprotected nanoparticles consist of

a $NaYF_4$ core which is capped with a 1 nm thick oleic acid layer to which DSPE-mPEG and DSPE-PEG-SH are attached. The ratio mPEG to PEG-SH is 10:1. The DSPE-PEG-SH was capped with the photoremovable group 2-bromo-4′- hydroxyacetophenone. This allows the thiol to be de-protected with triggered with UV light, which enables the nanoparticle to bind to a gold surface.

Other nanoparticles were used for testing purposes as they have consistent behaviour which can be used to confirm operation of the trapping setup. These particles include hexagonal boron nitride (hBN) nanoflakes and polystyrene nanospheres.

Chapter 4

Experiments

The experiments presented within this chapter show several of the steps that form a path to an integrated fiber-coupled erbium single photon source. First, the geometry of DNH apertures are tuned to maximize the brightness of erbium-doped nanocrystals so that nanocrystals with single erbium emitters can be detected and isolated. Second, discrete levels of emission are observed from dilutely erbium-doped nanocrystals, which are expected to correspond to the number of active emitters. Third, a photochemical method to anchor nanoparticles within a DNH aperture is presented with the goal to anchor trapped single emitters. Finally, the colloidal pattern transfer method is presented to fabricate integrated nanoaperture optical fiber tweezers.

The experiments presented in sections 4.1 and 4.2 aim to improve the emission enhancement and isolation speed of erbium-doped nanocrystals by using double nanohole apertures, building directly upon the optical trapping-based isolation method developed in our group by Alizadehkhaledi et al. [10], [13]. Section 4.3 explores a new method to permanently anchor trapped nanoparticles in place using phototriggered gold-thiol bonding of surface modified nanoparticles. The final experiment in section 4.4 investigates a low-cost method of producing nanoaperture optical fiber tweezers which builds upon work by Ehtaiba and Gordon in which similar devices were produced with a more costly template stripped method that

requires focused ion beam milling [53].

The results presented in sections 4.1 and 4.2 were originally written by M. Dobinson and have been published in the Journal of Chemical Physics and reprinted with permission of AIP Publishing [12]. Sections 4.3 and 4.4 are newly presented in this thesis and were written and performed by the author.

4.1 Optimizing DNH Geometry

The emission of Yb/Er-doped nanocrystals was measured for different cusp separations to find the optimal DNH geometry to maximize emission. The plasmonic resonances of the DNH aperture can be shifted by tuning the cusp separation so it was selected as the critical dimension to tune to maximize the enhancement [98], [99]. The optical trapping and emission measurements were performed with Yb–Er-doped nanocrystals with 18% Yb and 2% Er. These nanocrystals are bright compared to dilutely Er-doped nanocrystals which makes small changes in enhancement easier to detect. As these nanocrystals are of a comparable size and have near-identical absorption and emission wavelengths to the dilutely Er-doped nanocrystals studied in later experiments, they serve as a useful tool to tune the geometry using the upconversion emission.

4.1.1 Experiment

Apertures with cusp separations from 23–95 nm were fabricated, following the procedure detailed in section 3.4.1, to evaluate the effects of the DNH geometry on emission enhancement from the Yb–Er-doped nanocrystals. Scanning electron microscopy (SEM) was used to measure cusp separations and aperture diameters of the DNH apertures. Two sizes of nanocrystals, 16.9 ± 1.3 nm and $26.2 \pm$

2.7 nm were used to evaluate emission enhancement from a range DNH apertures and were dispersed in hexane in concentrations of 1.3×10^{12} and 5×10^{12} nanoparticles/cm^3 for trapping. The smaller nanocrystals were used to probe the enhancement for cusp separations from 23–45 nm while the larger were used for 32–96 nm. Using two sizes of nanoparticles also allowed the effect of the particle size on the emission enhancement to be observed.

The nanocrystals were optically trapped using the setup described in section 3.2. A 980 nm laser is used for both excitation and trapping of the nanocrystals. As the particles are dispersed in hexane, trapping is confirmed by oscillation shown in figure 3.2b. Spectroscopy was performed for visible wavelengths to compare the DNH geometries. NIR spectroscopy was also performed for limited events with the geometry that maximizes the emission to confirm emission at 1550 nm. The transmission signal from the APD as well as the spectroscopic measurements were recorded.

4.1.2 Results & Discussion

(Reproduced in part from [12], with the permission of AIP Publishing)

Figures 4.1a and 4.1b show the emission of a single Yb–Er-doped $NaYF_4$ nanocrystal trapped in a DNH aperture with 32 nm average cusp separation. Emission peaks are apparent in Fig. 4.1a near wavelengths of 400 nm, 550 nm, and 650 nm. Figure 4.1b shows the emission at 1550 nm of a single Yb–Er-doped $NaYF_4$ nanocrystal trapped in a DNH aperture, which we could not observe in our previous measurements [10]. The linewidth in Figure 4.1b is limited by the emission band of ${}^4I_{13/2} \rightarrow {}^4 I_{15/2}$ levels. Plasmonic resonances found in simulation are much broader. Because the 1550 nm peak is entirely the result of Er, it is not expected to vary

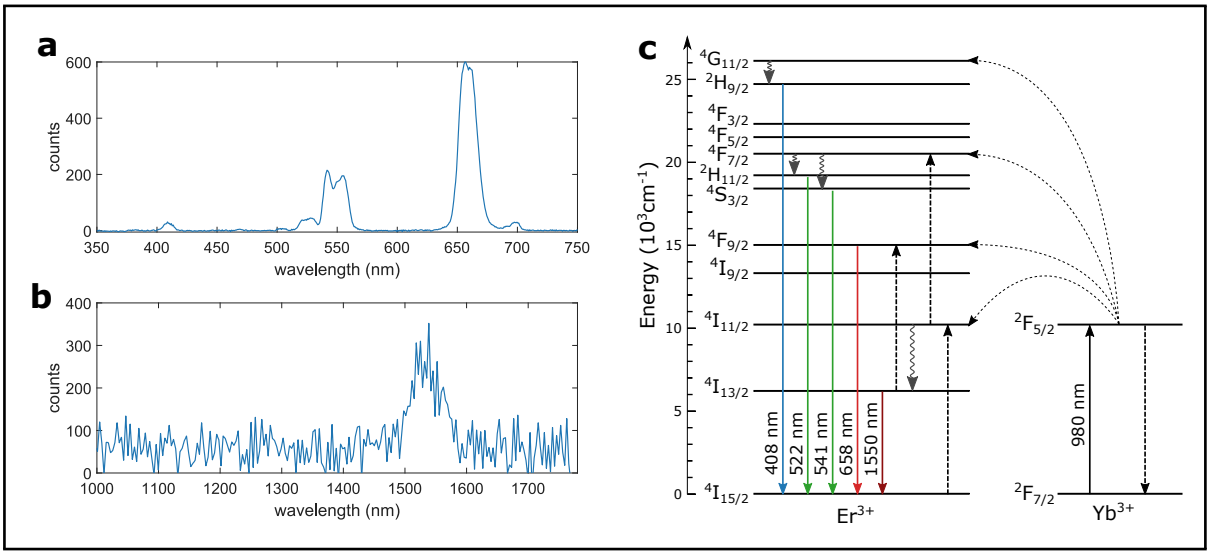

FIGURE 4.1: Measuring the emission spectra from single nanocrystals. (a) Upconversion emission spectra from a 26.2 nm nanocrystal observed for a sample with 32 nm average cusp separation. The counts can be compared for 400, 550 and 650 nm emission peaks. Collected by a spectrometer with a 10 ms acquisition time. (b) Downconversion emission spectra from a 16.9 nm nanocrystal observed for a sample with 32 nm average cusp separation. Collected by a spectrometer with 1 s acquisition time. (c) Schematic energy level diagram of Yb^{3+} sensitizer and Er^{3+} activator in nanocrystals. Radiative energy transfer (solid lines), non-radiative energy transfer (dotted lines), cross-relaxation (dashed lines), and multiphonon relaxation (curly lines). (Adapted from Suyver et al. [11])

significantly in linewidth due to the shifting plasmonic resonances with different nanoholes because the nanoholes show much broader resonances in this region of the spectrum.

We have not previously observed emissions at 400 nm and 1550 nm from single Yb–Er-doped $NaYF_4$ nanocrystals. The 400 nm upconversion emission is from the $^2H_{9/2} \rightarrow^4 I_{15/2}$ transition in erbium [11]. The 1550 nm downconversion emission is from the $^4I_{13/2} \rightarrow^4 I_{15/2}$ transition [7]. These transitions can be seen in the energy diagram shown in Figure 4.1c. Observing these two transitions from single nanocrystals for the first time in our group is possible due to the higher enhancement achieved using the double nanoholes.

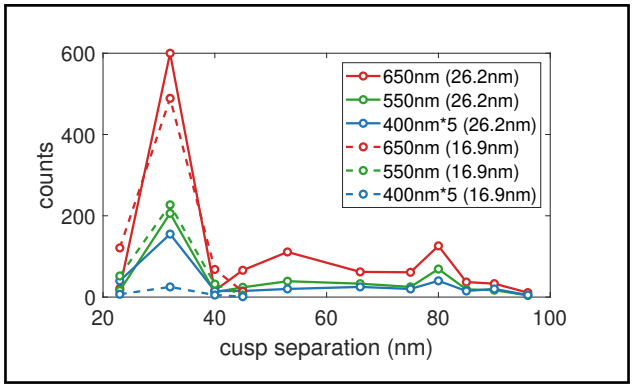

FIGURE 4.2: Investigating the influence of the DNH cusp separation on emission enhancement. Emission from 17 nm and 26 nm nanocrystals at 400 nm, 550 nm, 650 nm for varying DNH cusp separations. Emission counts at 400 nm are multiplied by 5 for visibility.

Figure 4.2 shows the emission of the two sizes of Yb–Er-doped $NaYF_4$ nanocrystals using DNH apertures with varying average cusp separations. It illustrates how the size and shape of the aperture can impact the overall emission. Several measurements on different DNHs within each sample were taken to confirm that the measured emission is from a single trapped nanoparticle. The average of these single trapping events is taken to form the final count. The normalized standard deviation over different measurements of a single 26.2 nm nanocrystal was 2.4%,

4.3% and 6.5% and for a single 16.9 nm nanocrystal it was 3.3%, 5.6%, and 4.8%, for the 400, 550 and 650 nm emission. The laser power is maintained at ~9 mW (as measured before the 100× objective) to simultaneously excite the structure and trap the particle.

The emission and trapping characteristics of 26.2 nm Yb–Er-doped $NaYF_4$ nanocrystals are measured in ten different samples of DNH apertures with average cusp separations from 32 to 95 nm. We observe that the sample with 32 nm cusp separation has the largest emission and exhibits plasmonic resonance at additional wavelengths, 400 nm and 1550 nm, that are significantly larger than in apertures with other cusp separations. The emission was compared to previous results from our group which used the same experimental setup with rectangular apertures [10]. This aperture size showed additional enhancement factor of approximately 50, over the best rectangular aperture. With the 26.2 nm nanocrystals, enhancement at 400 nm can only be clearly seen in two samples–32 nm and 80 nm average cusp separation.

The 16.9 nm nanocrystals are used to probe the effect of smaller apertures as the 26.2 nm nanocrystals are too large to trap in DNHs with cusp separations under 32 nm. The 16.9 nm nanocrystals are too small to trap in DNHs larger than 45 nm, so the measurements for these were performed for four different samples of DNH apertures with cusp separations from 23 to 45 nm. It was seen that the 32 nm cusp size remained the peak, showing that it has optimal plasmonic resonance to enhance emission at 650 nm. There was one isolated case where a nominally 26.2 nm nanocrystal was trapped in a nominally 23 nm gap, which is possible given the size tolerances.

These results show that the resonance wavelengths shifts as the cusp separation changes. The colloidal lithography method used to prepare these samples adjusts

the cusp separation by changing the plasma etching time, this also affects the diameter of the apertures. Changing both the cusp separation and aperture diameter like this can impact both the enhancement factor and resonant wavelengths.

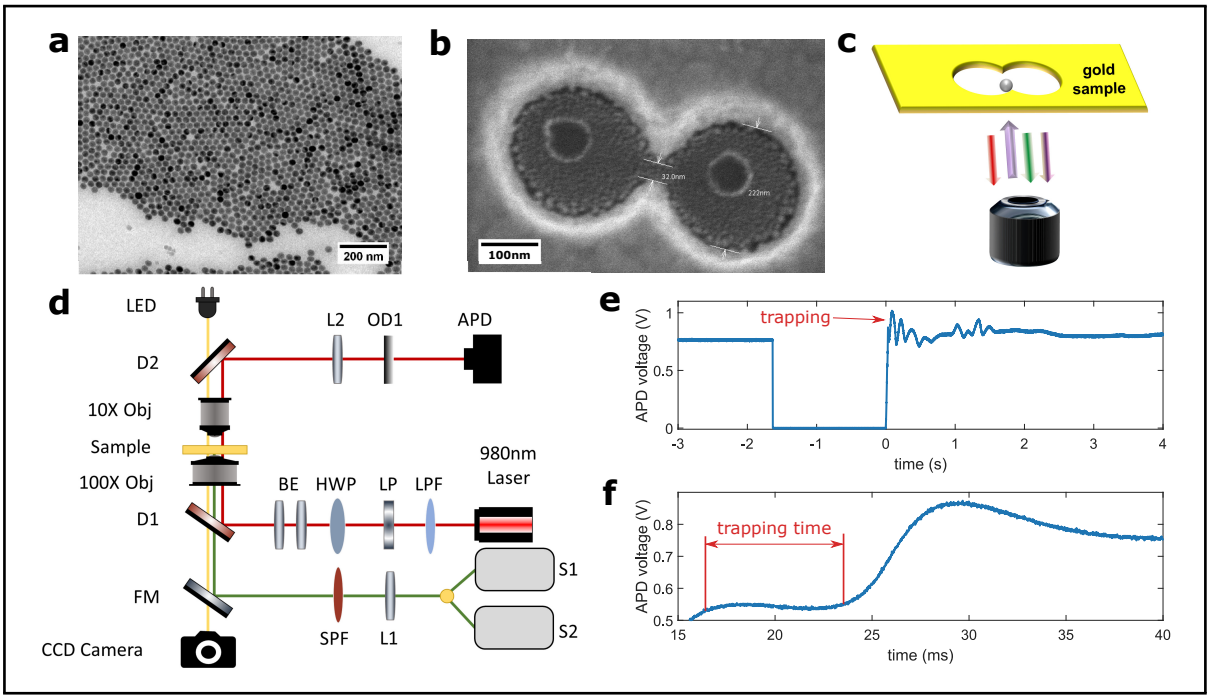

FIGURE 4.3: Optical trapping of Yb–Er-doped $NaYF_4$ nanocrystals with DNH. (a) Image of $NaYF_4$ nanocrystals with nominal diameter of 26.2 nm. (b) Image of a fabricated DNH structure with 32 nm cusp separation and 222 nm aperture diameter, taken with scanning electron microscope. (c) Schematic of a trapped nanocrystal in a DNH aperture on a gold sample. (d) Schematic of optical tweezer setup. (e) Optical transmission through a 32 nm DNH aperture in a metal film trapping a 26.2 nm nanocrystal, as measured by the APD voltage. Laser is turned on at 0 s. (f) Magnified region showing the APD voltage change shortly after the laser is turned on and trapping time measurement.

To probe this further we look at FDTD simulations (Lumerical FDTD ver. 2020 R2.3). The simulations calculated the electric field inside the cusp of the DNH structure where the particle would be trapped as shown in Fig. 4.3c. The structures were modeled from SEM images similar to Fig. 4.3b. A total of four different DNHs were modeled around the peak of interest at 32 nm cusp separation. Figure 4.4a

shows the simulated electric field intensity inside the cusp of a 32 nm DNH structure.

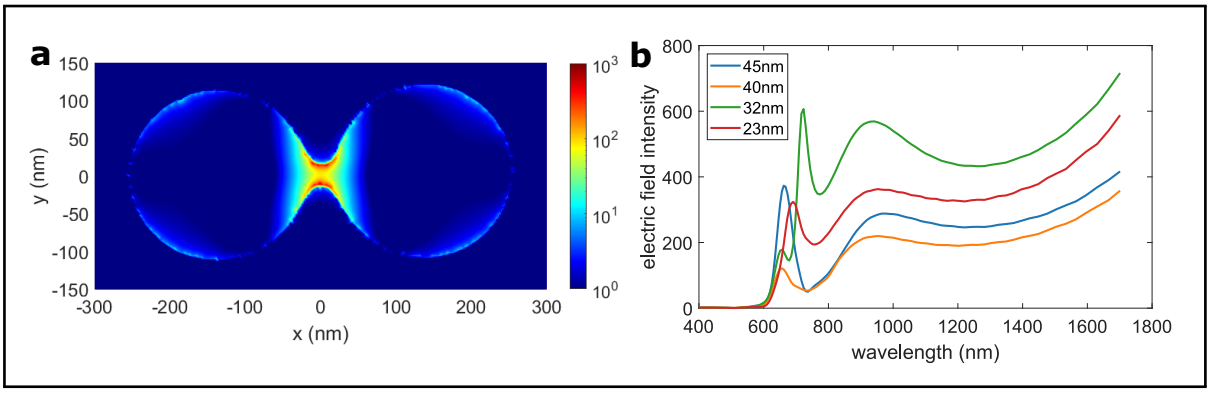

FIGURE 4.4: Simulated electric field intensity. (a) Visualization of the electric field intensity inside of a DNH with 32 nm cusp separation. (b) Electric field intensity for DNHs with 22.7 nm, 32 nm, 40 nm, and 45 nm cusp separations. Normalized to the incident intensity.

Figure 4.4b shows the simulation result of the relationship between the near-field electric field intensity (normalized to the incident intensity) and wavelength inside the cusp of DNH structure with different cusp separations. It can be seen that the 32 nm cusp separation has the greatest overall electric field intensity. There are two main resonant peaks for each of the simulated DNH structures. The structure with 32 nm cusp separation has peaks at 720 nm and 940 nm. The simulations were performed based on single SEM images and as the resonance frequencies are sensitive to the curvature of the cusps and the exact separation it is expected that the peaks differ slightly from the experimental results. The simulations show that multiple resonances can be used to enhance both excitation and emission wavelengths. There is minimal field enhancement seen in the simulations at 400 nm, but experimental results show increased overall emission at that wavelength. This suggests that the main effect is seen at the excitation wavelength, increasing the energy transfer, with additional resonances for other wavelengths.

4.2 Observing Discrete Emission Levels

This experiment measures the emission from optically trapped dilutely Er-doped $NaYF_4$ nanocrystals using DNHs with the geometry found in section 4.1 to maximize enhancement, a 32 nm cusp separation.

4.2.1 Experiment

The nanocrystals evaluated in this experiment have a nominal 2.48 Er/nanoparticle and a diameter of 22.7 ± 2.4 nm. The nanocrystals were dispersed in hexane with a concentration of 4×10^{12} nanoparticles/cm^3 for trapping. The visible emission was measured for 100 trapping events. It is expected that the distribution of the erbium ions in the nanocrystals follows a Poisson distribution. It is also expected that the emission will form discrete levels which correspond to the discrete counts of erbium ions present in the nanocrystals.

The setup described in section 3.2 is used for optical trapping. Excitation and trapping of the nanocrystals is by a 980 nm laser and the visible emission is collected. Trapping is performed in hexane and is confirmed by oscillation shown in figure 3.2b. The transmission signal from the APD as well as the spectroscopic measurements are recorded.

4.2.2 Results & Discussion

(Reproduced in part from [12], with the permission of AIP Publishing)

After finding that a DNH cusp separation of 32 nm shows the best enhancement with Yb-Er-doped nanocrystals, we applied this finding to search for and isolate nanocrystals with single erbium emitters. Dilute Er-doped $NaYF_4$ (with no

Yb) nanocrystals were produced with a nominal diameter of 22.7 nm (standard deviation of 2.4 nm) and a nominal number of Er ions per nanocrystal of 2.48. It is expected that the Er^{3+} ions are statistically distributed within the $NaYF_4$ crystals following a Poisson distribution with $\lambda = 2.48$. As the nanocrystals have varying numbers of Er^{3+} ions, we expect to see emission counts with levels corresponding to the different number of ions that follows a similar distribution. Trapping was performed for 100 events using a DNH with 32 nm cusp separation, measuring the emission spectrum for each event.

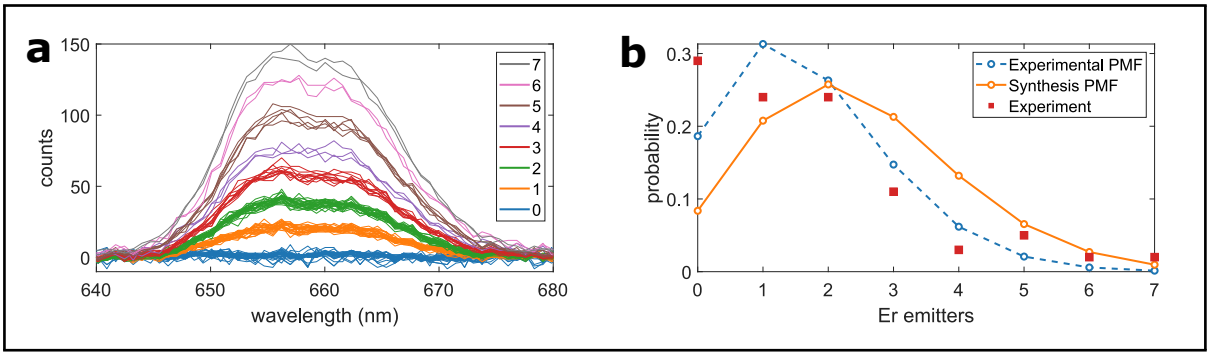

FIGURE 4.5: Measuring discrete emission levels from low counts of erbium emitters. (a) Emission counts from nanocrystals showing discrete levels corresponding to different amounts of active erbium emitters. Collected by a spectrometer with a 1 s acquisition time. (b) Poisson probability mass functions (PMFs) for the experimental ($\lambda = 1.68$) and synthesis ($\lambda = 2.48$) and experimental probabilities for the number of Er emitters.

Figure 4.5a shows the upconversion emission from 640 nm to 680 nm of single nanocrystals as measured with a 1 s integration time. It can be seen that the emission is separated into discrete levels. We attribute these levels to the discrete numbers of erbium emitters in the nanocrystals, from zero to seven individual active emitters. The integrated emission counts give a clear way to distinguish between the distinct numbers of active erbium emitters. The experiment demonstrated a mean of 1.68 ± 0.17 active erbium emitters per nanocrystal. Compared to the expected mean from the synthesis, this gives a yield of 0.67 ± 0.07 which is consistent

with previous findings from our group [13].

Figure 4.5b shows the probability distributions of Er emitters per nanocrystal as expected from the synthesis and experimental means. This distribution makes the assumption that all Er^{3+} ions can emit photons. However, it is expected that surface quenching significantly reduces the emission from Er^{3+} ions near the surface of the nanocrystal [43]. A quenched layer of 1 nm leads to quenching of 24% of the Er^{3+} ions in the volume. This seems to be a plausible explanation considering the statistical uncertainty in the experimental results.

The different DNHs were nominally the same and therefore showed the same emission intensity. The final Poisson distribution analysis used data from several different DNHs, each following the same discrete level response.

The emission measurements were collected with a spectrometer with a 1 s acquisition time. This is an improvement by over a factor of 40 compared to previous results from our group which required a 30 s acquisition time and produced even fewer counts [13]. This is consistent with the finding in Section 2 and makes it clear that DNHs can be used to improve the process of isolating single emitters. We believe that this level of enhancement will allow for detecting and isolating single emitters at 1550 nm; however, improvements in the optical setup for that wavelength are required.

4.3 Anchoring Nanoparticles

A photochemical method of anchoring erbium-doped nanocrystals inside of a DNH aperture was explored in this experiment. Surface-modified nanocrystals can be optically trapped in DNH apertures and a UV phototriggered reaction causes the nanoparticles to anchor in place. This experiment explores this novel technique as a step to isolating a single erbium emitter in a DNH for maximum emission.

Erbium-doped $NaYF_4$ nanocrystals can be synthesized with a polymer coating with a proportion of thiol end group which readily attach to gold. To prevent these from immediately attaching to the gold surface, they can are protected with a photoremovable group, 2-bromo-4'- hydroxyacetophenone. When exposed to UV light at 340 nm, this group disassociates from the nanoparticle, de-protecting the thiol group and allowing the particle to bind to gold.

A nanoparticle trapped in a DNH aperture is held close to the gold walls of the aperture by the high field intensity at the tips of the cusps [98], [99]. While the nanoparticle is trapped, a photochemical reaction can be triggered by UV exposure to bind the nanoparticle to the gold inside of the DNH aperture, anchoring it in place. Plastic substrates were used in this experiment as prior works have shown that plastic substrates have lower surface charge than glass substrates which also has benefits for trapping stiffness and time-to-trap [92]. It is thought that due to the lower surface charges the trapped particles are closer to the metal structure where the electric field intensity is highest, which is beneficial for anchoring.

This experiment was used as a first step to narrow down the wide range of variables in the anchoring process to make the procedure more repeatable and reliable. The optical power, cusp separation, and UV exposure time were varied in this experiment. More details on these parameters are listed below:

DNH Geometry The cusp separation & aperture diameter of a DNH aperture affects the local electric field intensity which dictates how close the nanoparticle is held to the gold walls of the aperture.

Optical Power Higher optical powers yield stiffer trapping and higher field intensity, which also controls how close the nanoparticle is held to the gold walls. However, the polymer coating on the nanoparticles and the PVC substrate are sensitive to heat and can be affected by excessive power.

Exposure Time A sufficient proportion of the nanoparticle's photoremovable groups must be exposed to the UV light for anchoring. Long exposure times can ensure that the photochemical reaction is triggered but it also may have negative effects such as anchoring multiple particles.

The optical trapping, anchoring, SEM imaging, and analysis were performed by Michael Dobinson. The DNH apertures were fabricated by Elham Babaei. The nanoparticles were synthesized by Adriaan Frencken of Dr. Frank van Veggel's group.

4.3.1 Experiment

A range of DNH apertures were fabricated using the colloidal lithography method discussed in section 3.4.1 with the modification of using 22×22×0.17 mm PVC cover slips rather than glass as the substrate. The apertures were fabricated using 200 nm polystyrene spheres with plasma etching to produce apertures with nominal cusp separations ranging from 30 to 85 nm. Photoprotected surface-modified $NaYF_4$ nanocrystals were synthesized as described in section 3.4.2. Three types of nanocrystals were synthesized: undoped $NaYF_4$ nanocrystals with photoprotected

thiol groups, $NaYF_4$ nanocrystals doped with a nominal 1.8 Er/NP with photoprotected thiol groups, and undoped $NaYF_4$ nanocrystals with a polymer-coating and no photoprotected thiol groups. The undoped nanocrystals were used in the initial anchoring tests. After confirming that UV exposure can trigger the anchoring, the doped nanocrystals were used in attempts to detect discrete emission levels to determine if the results from the experiment in section 4.2 could be applied to anchor nanoparticles with a specific doping level. The doped nanoparticles were also proposed to test if the emission varied between the trapped particle in solution and the particle when attached in the DNH out of solution. The nanocrystals with no photoprotected thiol groups were used as a control to confirm that the UV exposure was the catalyst for anchoring.

The nanoparticles solutions contained particles with a nominal diameter of 38 nm. The initial solutions had a nanoparticle concentration of ~10 $\mathrm{mg\,mL^{-1}}$ with an additional ~40 $\mathrm{mg\,mL^{-1}}$ of polymer micelles which had a diameter of ~12 nm. This high micelle concentration caused difficulties trapping so the solution was centrifuged to remove them. This also reduced the concentration of the $NaYF_4$ nanoparticles, yielding a final concentration of ~100 $\mathrm{\mu g\,mL^{-1}}$. This solution was used at both full concentration and diluted $10\times$ with deionized water for trapping. Prior to trapping the nanoparticle solution was sonicated for 10 minutes.

Optical trapping was performed with the setup described in section 3.2, with a green light source at 550 nm for imaging and UV light at 340 nm to trigger the photochemical reaction. Green light was used to ensure that the reaction was not triggered unintentionally, as 550 nm is far from the absorption band of the photoremovable group, which is expected to begin at wavelengths less than 360 nm [88]. The UV light was focused onto the DNH sample with the $10\times$ objective, with the light incident on the apertures passing through the gold film to expose the nanoparticles and the remaining UV light being blocked. Trapping and excitation

of the nanocrystals was performed using a single 980 nm laser with optical powers ranging from 2–30 mW, with some brief tests of up to 100 mW, as measured before the 100× objective. The polarization was rotated to maximize transmission through the DNH. Trapping was performed in water and confirmed by a jump in the transmission, similar to that shown in figure 3.2a. The UV source was activated using an electronic circuit for precise timing (see Appendix A). The transmission signal from the APD and the timing of the UV source were recorded. NIR spectroscopy was used to measure the downshifting luminescence of the erbium-doped nanocrystals. The DNH samples were imaged using SEM before and after anchoring.

The anchoring procedure was carried out by first optically trapping a nanoparticle, with the trapping confirmed by the transmission signal from the APD. To anchor the trapped nanoparticle, the UV source was activated to expose the sample for a specific duration. This exposure de-protects the thiol and allows it to bond to the gold on the inside of the DNH. Typical exposure times ranged from 0.5 ms to 20 s, with some test exposures of up to 10 mins. The trapping laser was maintained for a period after UV exposure to allow the thiol group time to bind to the gold.

The laser is then turned off and the DNH sample was released from the spacer and cover slip by a 12 h ethanol bath. Ethanol was used as it does not affect the PVC substrate, but requires a longer contact time than the acetone bath used for glass substrates. After release, the DNH sample was rinsed with ethanol and dried with nitrogen before imaging with SEM to confirm anchoring. Anchoring was confirmed by the presence of a nanoparticle with the correct 38 ± 3 nm diameter in the exposed DNH aperture. The previous SEM images of the DNH are compared to confirm that the particle is newly anchored and not a fabrication defect or contamination. The distance from the center of the exposed DNH to the nearest anchored nanoparticle was measured for nanoparticles that did not anchor within the cusp

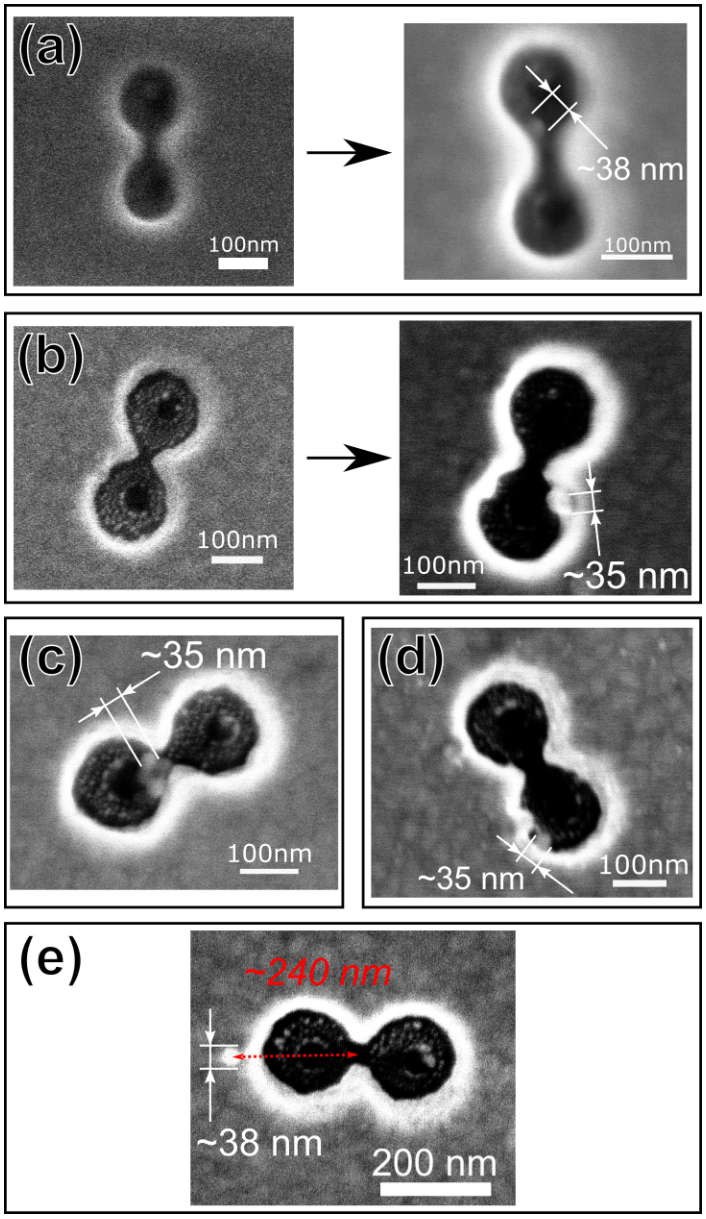

FIGURE 4.6: Attachment events of nanoparticles inside or near a DNH. (a) Single nanoparticle, 41 nm from center. 26 nm cusp separation, 9.5 mW power, 5s UV exposure. (b) Double nanoparticle cluster, 85 nm from center. 29 nm cusp separation, 4.5 mW power, 10 s UV exposure. (c) Multiple nanoparticle cluster in a DNH, 30 nm from center. 30 nm cusp separation, 4.5 mW, 20 s UV exposure. (d) Single nanoparticle, 152 nm from center. 45 nm cusp separation, 14.7 mW power, 6 s UV exposure. (e) Single nanoparticle outside of DNH, 240 nm from center. 36 nm cusp separation, 11.2 mW power, 6 s UV exposure.

region of the DNH. Nanoparticles closer than 2 µm from the exposed DNH were considered to be anchored as a result of the anchoring process. The yield was calculated for these cases as well as for anchoring within the DNH. A distance of 2 µm was chosen to give margin for the alignment of the laser with the aperture and is twice the diameter of the minimum spot size of the focused laser.

4.3.2 Results & Discussion

The photochemical reaction was successful in anchoring the nanoparticles to the gold surface. It was observed that exposing the the surface-modified nanoparticles to UV light caused them to anchor on the gold surface, which was not observed without UV exposure. The nanoparticles without the photoprotected thiol groups also did not anchor to the gold surface, with or without UV exposure. Out of a total of 98 UV exposure events, 39 events were successful in anchoring within 2 µm of the DNH. Of those 39 events, five resulted in the nanoparticle becoming anchored inside of the DNH aperture, a overall yield of 5%.

Figure 4.6 shows SEM images of anchoring events of single and clustered nanoparticles inside of and at the edge of DNHs. Before and after images are shown for the two anchoring events in figures 4.6a,b. The nanoparticle cluster in figure 4.6b consisted of two 38 nm particles stacked vertically with a small horizontal offset of ~5 nm while the cluster in figure 4.6c consisted of many 38 nm particles (four visible). It is not clear if the clusters are formed by multiple trapping during anchoring, or if they were present in the solution prior, despite sonication.

Figures 4.7a,b,c shows how the cusp separation, laser power, and UV exposure time were varied in this experiment and the resulting yields. Each parameter was adjusted see how they affect the anchoring process. The proportion of anchoring events within 2 µm is listed for each range. It can be seen in the first plot that

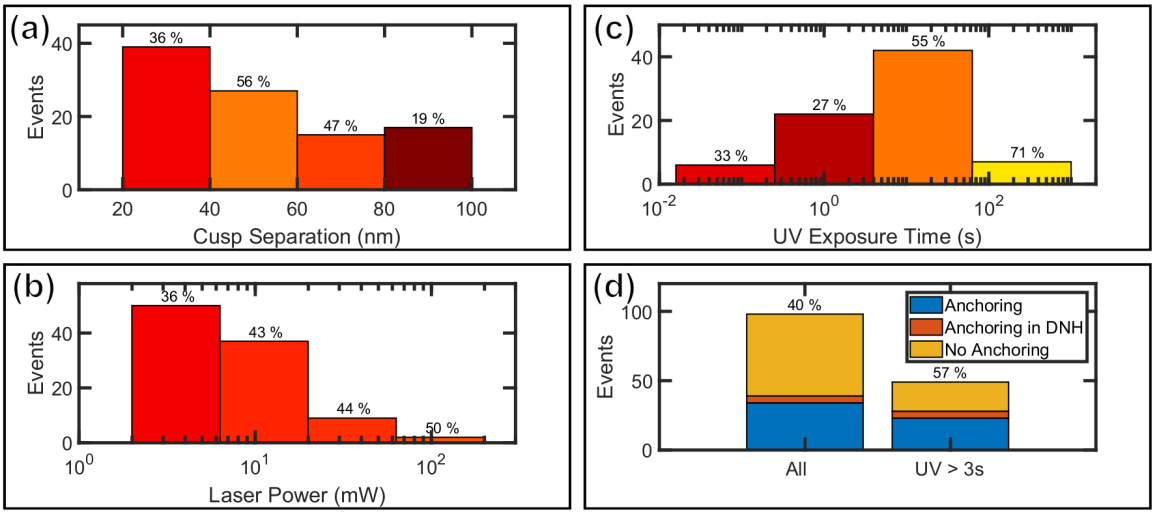

FIGURE 4.7: Distributions of the parameters controlled in the anchoring experiments showing the yield of particles attached within 2 µm for varying (a) cusp separation, (b) laser power, and (c) UV exposure time. (d) Total yield of nanoparticles attached within 2 µm of the DNH shown for both all events as well as for a subset with UV exposures above 3 s.

apertures with cusp separations above 80 nm had a low yield of 19%, while the best yield of 56% was seen for the 40–60 nm range. The second plot shows that the laser power did not have a significant influence in the anchoring success, with only a slight increase in yield for higher powers. The final plot shows a clear improvement for longer UV exposure times, with exposures under 4 s having 30% yield which increases up to 71 % for exposures above 64 s. It is worth noting that the typical ranges for anchoring events that occurred inside of the DNH differed slightly. In those events, cusp separations were from 23–45 nm, power ranging from 4.5–15 mW, and UV exposure times between 5–20 s.

Figure 4.7d shows the attachment yield for the photochemical anchoring process. Approximately 40% of the 98 total events showed the nanoparticle attaching within 2 µm of the DNH aperture. As shown in figure 4.7c, the data made it clear that short UV exposure times were not sufficient for anchoring. The yield increases to 57% when the range is limited to anchoring events which used UV exposures

over 3 s.

Overall, no events resulted in the nanoparticle anchoring in the middle of the cusp region as expected. The majority of anchoring events resulted in the nanoparticle anchoring outside of the DNH, but within 500 nm of the cusp region. The reason for this behaviour is unknown but there are several possible causes that can be investigated. Following the completion of the experiment, it was realized that the polarization for maximum transmission is not consistent with the polarization for maximum field intensity for 980 nm excitation of DNHs [100]. As the polarization used for trapping was set for maximum transmission, the position of maximum field intensity is not certain which may be a factor in the attachment positioning. Another possible cause may be the nanoparticle being released before the thiol can bond to the gold. Self-assembled monolayers (SAMs) are based similar thiol reactions which have adsorption times reported over a wide range, from milliseconds to hours [101]. In future experiments, the laser dwell time after exposure should be controlled to evaluate this parameter. Finally, there is a chance that prolonged UV exposure can inhibit adsorption or even destroy the bond after forming. The Au–S bond can be delicate as the thiol bond changes from a weak physisorbed bond to a strong chemisorbed bond. This takes some time and requires a well-prepared surface and in some cases the bond does not become chemisorbed [87], [102]. Thiol bonds have also been reported to have a mobility which can lead to diffusion away from the initial bonding point, although this is a slow process [86]. The energy of UV light has also been shown to cause oxidation of SAMs in some cases and can cause C–S bond scission [103], [104].

4.4 Fabricating Nanoaperture Optical Fiber Tweezers

A low-cost method to fabricate nanoaperture optical fiber tweezers (NAFT) using colloidal pattern transfer is explored in this experiment. These devices consist of a DNH aperture in a thin gold film which is aligned with the core of an optical fiber. The final device can be used in an all-fiber setup for optical trapping where the tip is dipped in the analyte. This all-fiber setup can remove the challenging alignment requirements of conventional nanoaperture optical trapping.

The colloidal pattern transfer method transfers DNH apertures in a gold film, which are fabricated by colloidal lithography, to the face of a cleaved optical fiber. An optical setup is used to align the core of the fiber and the DNH, which is followed by bonding with UV-cured optical adhesive and lift-off of the fiber to detach the gold from the substrate. This device can then be connected to a fiber-based optical trapping setup.

This experiment was limited in scope and served as a proof-of-concept for the colloidal pattern transfer technique. This technique was used to fabricate NAFTs for trapping polystyrene nanospheres, hexagonal boron nitride, and erbium-doped nanocrystals. Several modifications to the DNH fabrication process were required to produce suitable apertures and a specialized optical setup was designed for aligning and attaching DNH apertures to an optical fiber. Two fiber-based trapping setups were also made for this experiment for trapping in transmission and reflection modes.

4.4.1 Experiment

The colloidal lithography method presented in section 3.4, with minor modifications, was used to fabricate DNH apertures. No Ti adhesion layer was used to facilitate removal of the Au film from the glass substrate. The DNH samples used

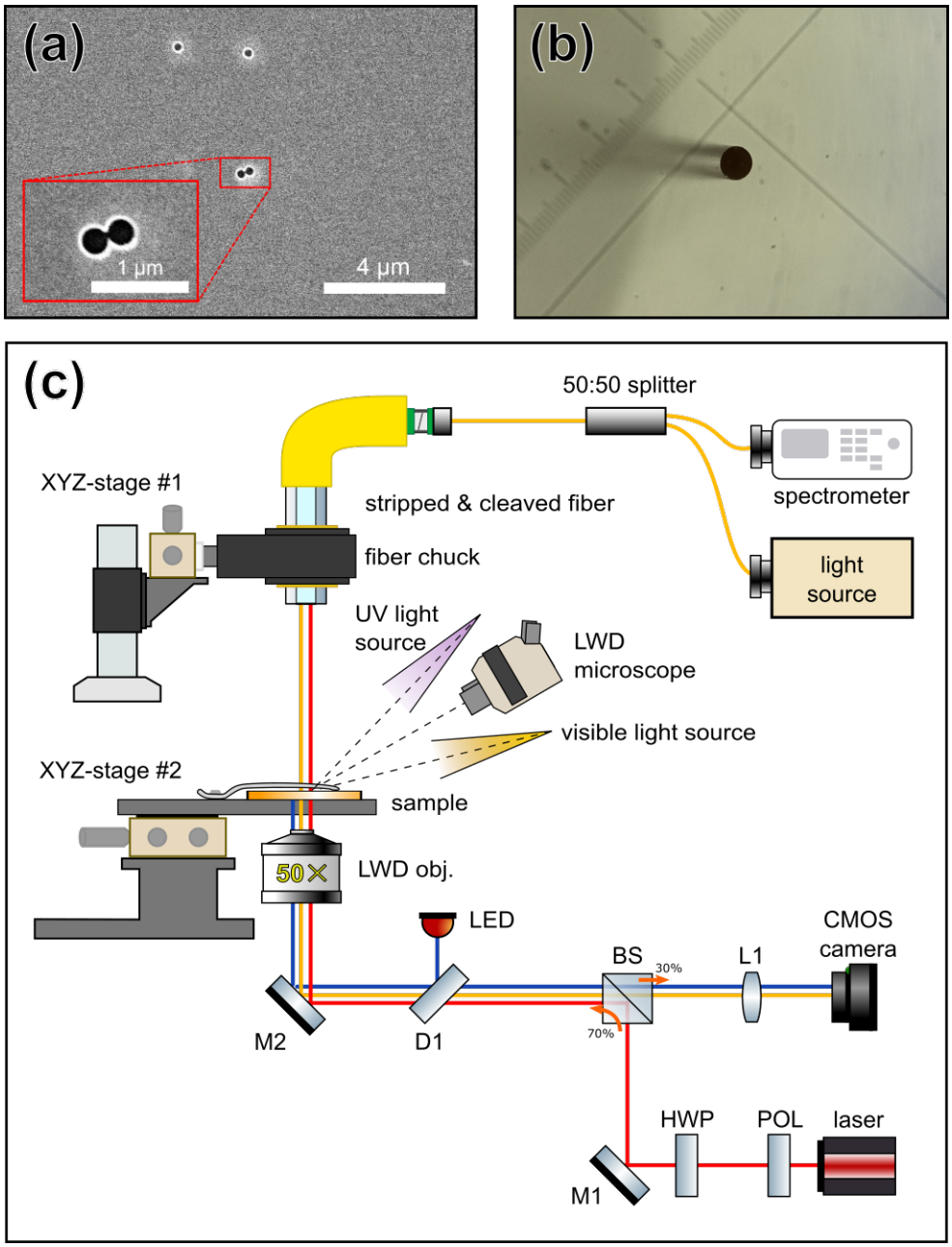

FIGURE 4.8: The fiber attachment process. (a) Scanning electron microscope (SEM) image of a DNH aperture used to fabricate a NAFT. (b) Image of the face of a cleaved fiber taken through a microscope with 50× magnification. (c) Schematic of the optical setup used to fabricate the nanoaperture optical fiber tweezers.

in this work were fabricated using 300 nm polystyrene spheres in a solution of 0.001% w/v with no plasma etching. This is a more dilute solution than typically used and results in a sparse distribution of apertures with few DNHs. The sparse distribution is desirable as the DNH chosen for fabrication must be separated from all other apertures by at least the fiber core's radius to avoid crosstalk, 4.1 µm for single-mode fiber. After sputtering, the DNH samples were briefly sonicated in ethanol until the gold started to detach from the glass substrate, 3–8 minutes. The sonication process damaged the gold surface, however it is necessary to detach the polystyrene spheres and large areas of the gold surface remained usable. The resulting samples yielded DNH apertures with cusp separations of 68 ± 9 nm with diameters of 268 ± 15 nm.

Figure 4.8a shows an image of a suitable DNH for fabrication a NAFT with the colloidal pattern transfer method, captured with a scanning electron microscope (SEM). The sparse distribution of apertures required for the process resulted in the likelihood of apertures being DNHs rather than single holes was very low. SEM was used to find viable DNH apertures to fabricate the NAFT devices, however this can also be done without SEM using polarization and transmission analysis [92].

Figure 4.8b is a microscope image taken with 50× magnification of a cleaved fiber face, taken during inspection. This fiber was acceptable and a NAFT was fabricated on it with the colloidal pattern transfer method.

Figure 4.8c shows the optical setup used to fabricate the NAFTs using an inverted long working distance microscope with a laser and light source for imaging and precise alignment. The setup consists of an 850 nm laser which is collimated using a FiberPort (Thorlabs, PAF-X-7-B) and polarized before passing through a 70:30 beamsplitter (Thorlabs, BS023) and focused on the sample with a long working distance 50× microscope objective (Mitutoyo, 50× Plan Apo SL). A cleaved single-mode optical fiber with the jacket removed and the coating stripped is held

above the sample in a fiber chuck (Newport, FP-1). The other end of the fiber connects to a 50:50 1×2 fiber splitter (Thorlabs, TM200R5F1B). One path of the fiber splitter is connected to a spectrometer (Ocean Optics, USB4000) with the other path being illuminated by a focused white light source. A 20 dB fiber attenuator was used when working with higher laser powers to protect the spectrometer. The fiber chuck and the sample are held on separate three-axis stages for alignment. A CMOS camera (Thorlabs, DCC1645C) in the reflection path of the beamsplitter is used to image the sample. An LED light source enters the beam path by a short-pass dichroic mirror (Thorlabs, DMSP1180R) that reflects ~50% of visible light and passes ~90% of light at 850 nm. A long working distance microscope (Wild, M5A), mounted on a swing-arm stand, and a visible light source are used to observe the surface of the sample. A UV light source is used to set the UV-cured optical adhesive.

The colloidal pattern transfer method is used to fabricate NAFTs by aligning the core of a cleaved fiber with a DNH aperture in gold film fabricated by colloidal lithography. A UV-cured adhesive is used to transfer this gold pattern to the fiber tip. Careful preparation of the optical fiber is critical for success. The following describes the procedure in detail:

1. Preparation The DNH aperture sample is affixed to a plain glass slide with the gold side facing upwards using an adhesive spacer before being placed in the inverted microscope. The sample is moved to find the DNH of interest by translating XYZ-stage #2 using constellation mapping combined with SEM images, or polarization and transmission analysis. In this step it can be helpful to illuminate the sample from the top with a visible light source.

2. Fiber Cleaving A single-mode optical fiber (Corning, SMF-28) with an FC/APC connector is first scissor cut to a length of at least 2 m. Approximately 20 cm

of the jacket and strength member are then removed. The 242 ± 5 µm buffer-/coating layer is removed by stripping the fiber with a stripping tool (Clauss, NN254). This reveals the fiber cladding with a 125 ± 0.7 µm diameter. The bare fiber is cleaned with isopropyl alcohol and then cleaved (Sumitomo, FCP-22L). The cleave is examined with a microscope from the side to ensure that it is flat. The face of the cleave is also examined (fig. 4.8b) to ensure that there are no visible marks from the cutting blade that go deeper than 10% of the face diameter. It is critical that this cleave is performed correctly as any contaminants can affect the bonding to the gold. The fiber is re-cleaved if found to be inadequate. The cleaved fiber is then carefully loaded into a fiber chuck.

3. Alignment The optical fiber is then aligned with the DNH by maximizing the transmission of the laser into the optical fiber using the spectrometer, as well as by viewing the light emitted from the fiber on the camera. This is done by translating the fiber using XYZ-stage #1, keeping the sample fixed. Adequate coupling for rough alignment is typically achieved with the fiber tip within 200–500 µm of the gold surface. The angle of the fiber face is important to maximize coupling and can be adjusted using the fiber chuck. Care must be taken to ensure that the fiber tip does not contact the gold surface. In this step, the polarization of the laser can also be changed to observe a change in the transmission through the fiber to confirm that it is aligned with a DNH.

4. Bonding After alignment, the fiber is lifted from the sample by raising XYZ-stage #1. A ~1 µL drop of UV-cured optical adhesive (Norland Products, NOA 61) is pipetted onto a clean glass slide. The adhesive is carefully applied to the tip of the cleaved fiber by dipping the fiber into the drop. The excess adhesive is removed by carefully bringing the adhesive on the face of

the fiber in contact with the clean glass slide. This is repeated until minimal adhesive is present on the fiber face, monitored using the LWD microscope. The optical fiber is then lowered back to the previous position on the gold DNH sample so that the adhesive barely contacts the surface. The alignment of the fiber may have changed during this process so the position of the fiber should be re-adjusted for maximum transmission. Once aligned, the adhesive is cured for a minimum of 5 minutes with an external UV light source.

5. Release The fiber is slowly lifted directly upwards using XYZ-stage #1 to release the gold from the glass surface. Care must be taken with the finished device as it is delicate and can be damaged during handling and cleaning.

6. Inspection The fiber is kept mounted in the inverted microscope while the DNH sample is removed. The camera is used to confirm that the gold has not shifted off of the core region during release. The laser can also be used to confirm that the transmission levels and polarization dependence have not changed significantly from before attachment. Following inspection, the NAFT can secured in a protective housing and connected to a fiber-based setup for trapping.

4.4.2 Results & Discussion

The colloidal pattern transfer technique was used to successfully fabricate NAFT devices which were used to trap polystyrene and hexagonal boron nitride nanoparticles in transmission mode. Trapping of erbium-doped nanoparticles in hexane was also attempted in reflection mode but no emission at 1550 nm was observed, although there was a small difference in the APD signal compared to pure hexane.

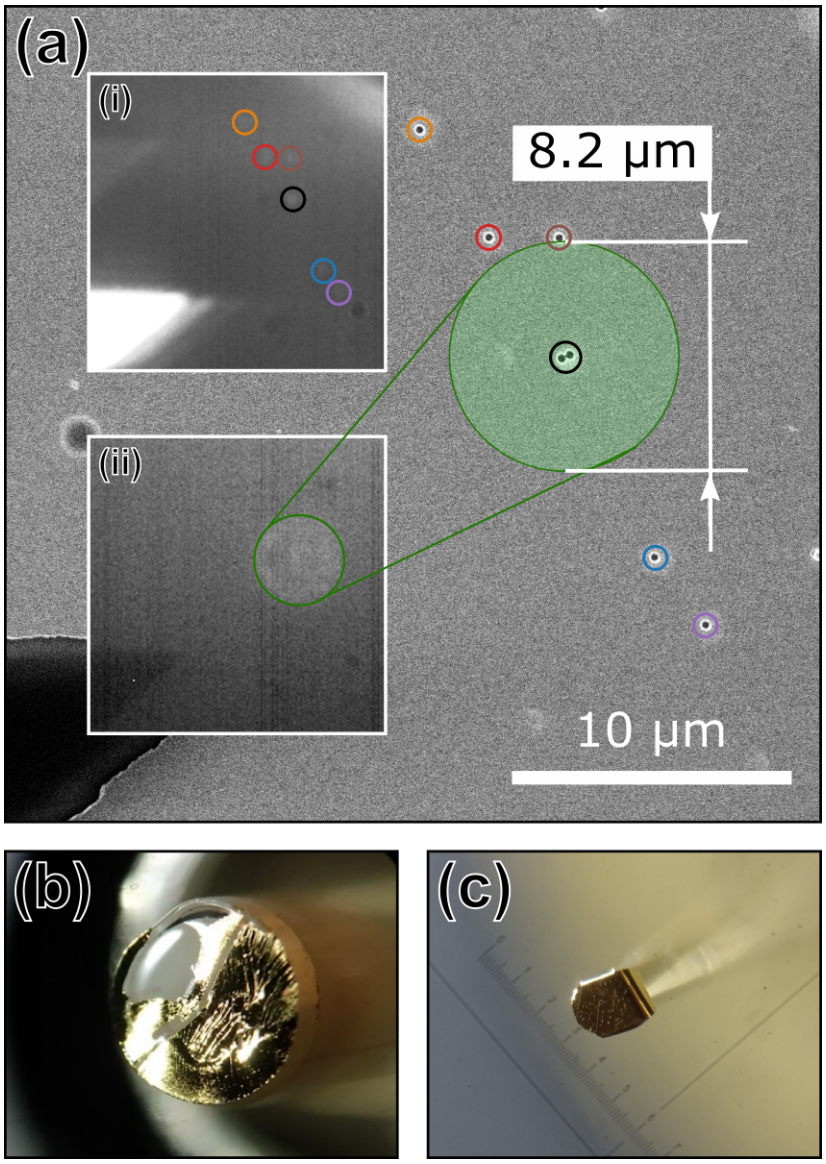

FIGURE 4.9: (a) Diagram showing alignment of the 8.2 µm fiber core with a DNH aperture found using SEM. Constellation mapping is done to find the DNH, the top inset (i) shows a camera image taken by transmitting light through the sample with the coloured circles matching the apertures between the camera and SEM images. The bottom inset (ii) shows the illuminated fiber core visible through the sample, with the surface being illuminated in reflection. The relevant area on the SEM image is shown with the green circle. (b) An unsuccessful fiber attachment using an FC/PC connector with a ferrule. (c) A successful fiber attachment on a cleaved fiber, with excess gold visible around the edges of the fiber.

While the fabrication of the NAFT devices was challenging, the fiber-based optical trapping setup required minimal tuning could be set up for trapping quickly which allowed for easy evaluation of the NAFTs.

Significant effort was required to find good DNH candidates as the sparse distribution yielded mostly single nanoholes with few DNHs which were challenging to find with SEM. This step has much room for improvement as it is possible to find DNH apertures using the laser in the inverted microscope setup shown in figure 4.8 by varying the polarization and monitoring the response in the transmission signal [92]. This process has potential for automation which could yield significant advantages for fabrication time.

Figure 4.9a shows how the optical fiber is aligned with a DNH aperture on the sample. The main image was taken using SEM to find a suitable DNH for fabrication. The large green circle marks the size of the fiber core and it can be seen that there is sufficient space for the DNH to be bonded without crosstalk. The scratch in the bottom left served as a fiduciary mark so that it could be found using the camera. Constellation mapping was used to confirm the location of the DNH, as shown in the top inset, by shining a light through the top of the DNH sample and observing the apertures with the camera. The matched DNH apertures are indicated in the figure using rings with matching colours. The bottom inset shows the same area but with the top light source removed and the core of the optical fiber visible as a circle of light which transmits through the gold. The lower LED is used to illuminate the surface slightly for alignment. This circle of light from the core is only visible when the optical fiber is within approximately 200–500µm of the gold surface.

Initial fabrication efforts focused on using fibers with prepared FC/PC connectors rather than cleaved fibers. This was intended to reduce the preparation work required, but the size of the ferrule lead to severe warping of the gold surface upon

release. Due to the large surface area of the ferrule and the inconsistent adhesion of the gold to the glass substrate, some areas would lift off sooner than others during release, leading to warping and tearing of the gold. The slightly convex face of the FC/PC connector may have also contributed to the release issues, this could potentially be mitigated by flat polishing before fabrication. The ferrule also limited the UV exposure in the center of the fiber which in some cases caused areas to not cure fully, even with long exposures.

Figure 4.9b shows an attempt using a ferrule where the gold surface was damaged during release. Ridges and tears caused by the release are clearly visible under a microscope with 50× magnification. Further inspection of this device, by observing the light transmitted through the core with the inverted microscope, revealed that the core and DNH were no longer aligned and was unusable.

Figure 4.9c shows the face of a NAFT after the release process. The smaller surface area of the cleaved fiber did not cause warping or tearing on release. Minor peeling of the gold outside of the fiber region is visible, which was common but this does not affect operation in most cases and can be trimmed if desired.

The fabrication process was challenging as it requires precise alignment and careful manual movement of all stages. The critical step in the colloidal pattern transfer process is translation of the fiber to meet the gold surface for bonding after applying the adhesive. The position must be closely monitored with the microscope to ensure that the adhesive only barely contacts and does not press into the gold surface. The epoxy is viscous and kept out of the DNH apertures by surface tension, but this action can cause epoxy to be enter into the DNH. Damage to the surface or the fiber core can also occur in severe cases. Several attachment attempts appeared successful as the DNH aperture was cleanly detached and remained aligned with the core, but they could not be used for trapping. This may be due to the UV-cured epoxy filling the DNH aperture when the fiber contacts the

surface.

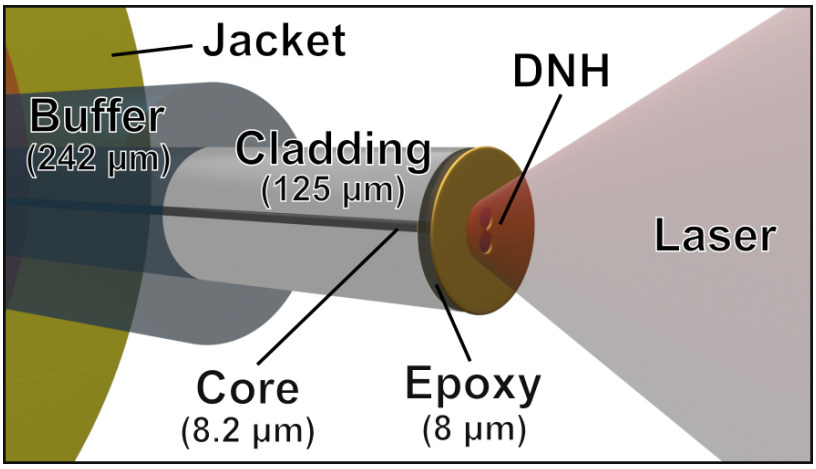

FIGURE 4.10: Schematic of a NAFT showing a DNH aligned with the core being illuminated with a laser (DNH enlarged to show features).

A NAFT was fabricated using the DNH shown in figures 4.8a and 4.9a with the colloidal pattern transfer technique. Figure 4.10 shows a model of a NAFT with the relevant features and dimensions. This device was used to successfully trap 40 nm polystyrene nanospheres and hexagonal boron nitride (hBN). Trapping in hexane was also attempted with Yb/Er-doped $NaYF_4$ nanocrystals, although neither a clear trapping signal nor emission at 1550 nm was observed. Between each trapping event, the device was cleaned by gently soaking in acetone followed by ethanol and then let dry. The fabricated devices were found to be delicate and care was taken during handling and cleaning. Contact of the gold on the fiber face with any solid surface caused immediate damage. The stripped section of the optical fiber is also prone to damage.

Figure 4.11a shows the optical setup used for trapping nanoparticles with the fabricated NAFT in transmission mode as well as trapping events with 40 nm polystyrene spheres and hBN. This setup allows for the laser to remain in fiber until reaching the DNH aperture with no alignment required. In this work, a fiber-coupled 980 nm laser (JDS Uniphase, SLDO-27-7552-160-LD) with a 980 nm fiber

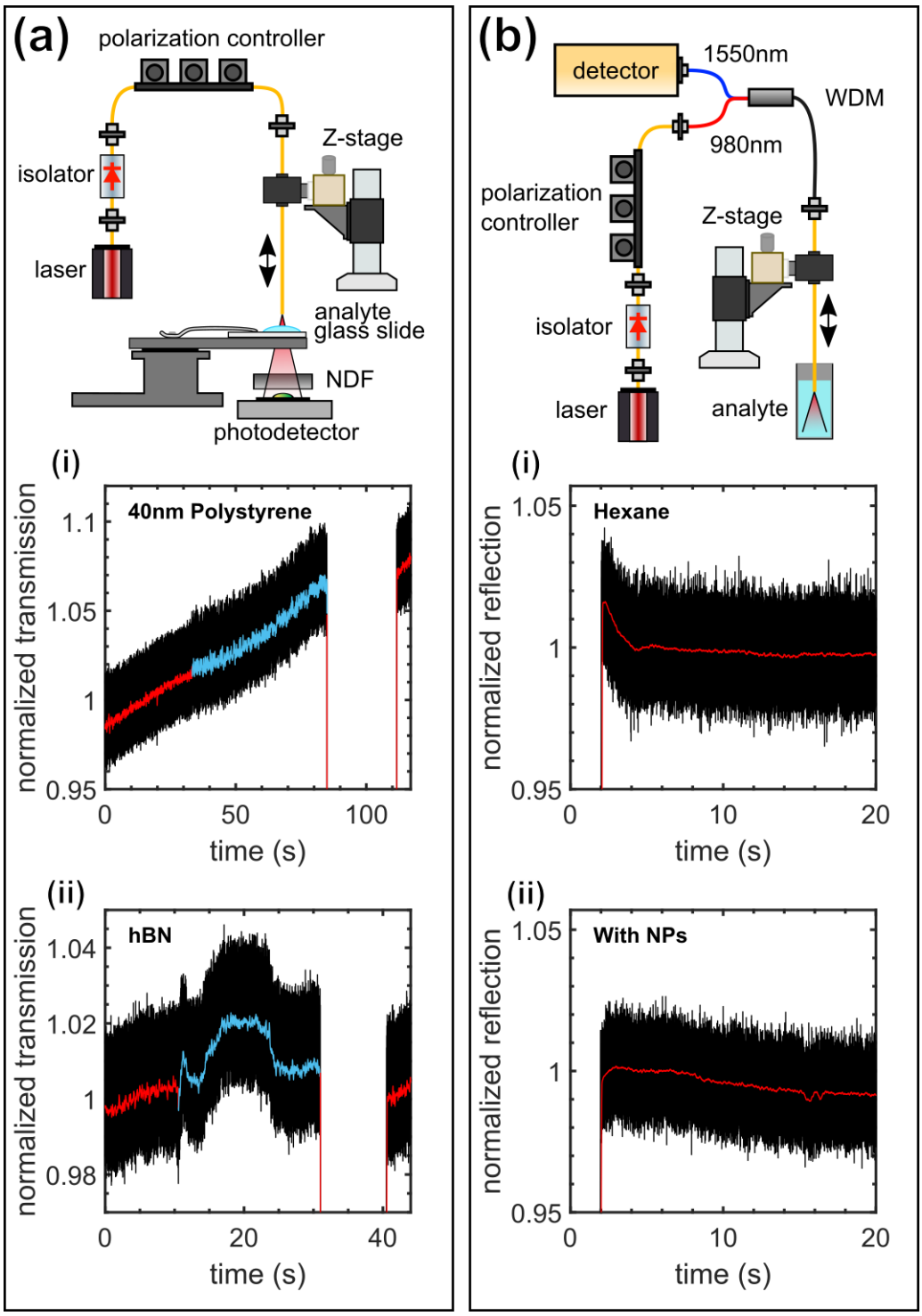

FIGURE 4.11: Schematic of trapping setups used with a NAFT, and trapping events recorded using each setup. The blue part of the line indicates trapping while the red part indicates no trapping. (a) Transmission mode setup monitors trapping with a femtowatt photodetector. (i) Trapping of 40 nm polystyrene and (ii) hexagonal boron nitride (hBN) are shown. (b) Reflection mode trapping setup uses a WDM split the reflected emission at 1550 nm from trapped erbium doped nanocrystals for detection. Events from (i) hexane and (ii) erbium-doped nanoparticles dispersed in hexane are shown.

isolator (Thorlabs, IO-F-980APC) connects to a fiber polarization controller before transmitting through the DNH aperture on the fiber tip. The fiber is mounted to a Z-stage so that it can be dipped into the analyte for trapping. The transmission is measured using a femtowatt photodetector placed below the sample, with a neutral density (ND) filter to limit the light received and prevent saturation. The polarization can be adjusted with the polarization controller to maximize transmission for the DNH. To optically trap with this setup, a glass slide is prepared with a 0.12 mm thick adhesive spacer (Grace Bio-Labs, SecureSeal) filled with 10 µL of the analyte. The slide is placed in the slide holder and the optical fiber is lowered to contact the solution using the Z-stage. The laser is turned on with low power and the polarization is adjusted for maximum transmission. The power is then increased for trapping. A DAQ is used to measure and record the transmission signal from the femtowatt photodetector.

Two trapping events observed using the fabricated NAFT are shown in figure 4.11a. The first trapping event was observed using a 0.1% w/v solution of 40 nm polystyrene nanospheres. The second trapping event was observed for a 5.4 $\mu g\,mL^{-1}$ solution of hexagonal boron nitride (hBN). The laser power was maintained at ~50 mW for both events, as measured after the isolator. The untrapped state is shown in red and the jump and increase in the variation indicates the transition to trapping, shown in blue. After the laser is turned off at and back on at, the signal returns to the untrapped state, as seen by the low variation. The trapping setup was sensitive to movement and small changes in the height of the fiber above the femtowatt photodetector corresponded to large signal changes. There was drift in the signal observed during long recording periods which appeared to be caused by drift in the Z-axis of the stage. These trapping results are consistent with prior work by Ehtaiba and Gordon [53].

Figure 4.11b shows the optical setup used for trapping erbium-doped nanoparticles with 1550 nm fluorescence in reflection mode. This setup is similar to that shown in figure 4.11a with the removal of the photodetector and addition of a 1×2 980/1550 nm wave-division multiplexer (WDM; Thorlabs, WD9850AB) in the reflection path with a detector. The WDM has low insertion loss and allows the 980 nm laser to excite the DNH for trapping with 19 dB isolation from the reflection path. The detectors used were either a spectrometer directly coupled to the fiber (Agilent, 86142B) or an APD (Thorlabs, APD120A), connected using a fiber collimator (Thorlabs, F220APC-1550). With this setup, the reflected laser light as well as the fluorescence of trapped particles can be used to detect when trapping occurs. As the isolation of the WDM is not perfect, a small proportion of the 980 nm laser signal is reflected into the 1550 nm arm. This is beneficial for reflection mode measurement with the APD, but it can be a problem for spectroscopy or photon counting. If more sensitive applications are required, a second WDM can be used to further remove the 980 nm component. To optically trap with this setup, a vial is filled with analyte into which the NAFT is dipped into by translating the Z-stage. The laser is turned on with low power and the polarization is adjusted for minimum reflection. The power is then increased for trapping. When using an APD, a DAQ is used to measure and record the reflection signal.

Optical trapping of 26.2 nm doped $NaYF_4$ nanocrystals (18% Yb, 2% Er) in reflection mode was attempted, yielding the result shown shown in figure 4.11b. The laser power was maintained at ~50 mW for both events, as measured after the isolator. This measurement was performed with the APD and fiber collimator to measure the reflection from the DNH. The first plot shows a control attempt in pure hexane where a brief jump in the reflection is seen when the laser is turned on before settling to a nominal value. This behaviour was consistent for hexane. When trapping the $NaYF_4$ nanocrystals in hexane, the large jump seen for pure

hexane was not observed, rather the signal appears to rise relatively slowly. Similar behaviour has been observed by others but measurement with a spectrometer showed no emission at 1550 nm [105]. These results are not conclusive as the coupling of the nanoparticle emission is poor and may not be easily detectable.

The observed fiber-based trapping events showed a minimal jump in the transmission compared to typical results for comparable apertures in an inverted microscope trapping setup (fig 3.1). With 40 nm polystyrene, a jump of 0.2% was observed in the fiber trapping event, compared to typical jumps of 3–5%. In a typical trapping setup, the laser is convergent and tightly focused to a beam spot of a few microns. In fiber-based trapping, the laser is approximately Gaussian inside of the 8.2 µm core and diverges as it exits the fiber. The DNH aperture lies approximately 8 µm away from the fiber face due to the epoxy layer [53]. The beam area increases over this distance as it diverges, lowering the power density. The area of the DNH aperture is small compared to the beam area, resulting in a large proportion of the light hitting the gold interface rather than passing through the DNH. The 70 nm gold layer used in this experiment is not opaque to 980 nm light, approximately 0.05% is transmitted [106]. This can be a significant proportion of the transmitted light which adds to the background of the signal transmitted through the DNH. A large background level reduces the size of the jump as a proportion of the total signal, and may be responsible for the observed difference, although further investigation is required to confirm this.

Due to time constraints, only a single device was successfully fabricated which was able to repeatedly trap nanoparticles. A total of sixteen other devices were fabricated but trapping was either not achieved or was not repeatable with these devices.

Chapter 5

Evaluation & Comparison

The experimental results presented in chapter 4 show that these methods have potential and could lead to an integrated fiber-coupled single photon source with further development. Tuning the DNH geometry to enhance the emission allowed discrete emission levels to be observed, but the nanoparticle anchoring and fiber attachment techniques need further refinement to significantly improve yield and reduce the fabrication time. Before these techniques are combined, the photon characteristics of the erbium-doped nanocrystals should first be evaluated, both with and without the surface modification.

Observation of discrete emission levels from erbium-doped nanocrystals is a promising result which shows that nanocrystals containing specific numbers of active emitters can be isolated out of solution using optical trapping. This is a distinct improvement over both the post-processing and ion implantation methods discussed in section 2.4 as it can be performed in real-time and particles without active emitters can be easily ignored. With the 1 s integration time used in this experiment, single emitters can be isolated in seconds which has enormous potential for combination with the photochemical method to anchor the emitter in place after detection. This rapid detection time was made possible by the significant emission enhancement from the tuned DNH apertures, substantially increasing the emission rate to a level detectable in seconds.

While these isolated nanocrystals may contain single active emitters, this has not yet been confirmed using HBT interferometry to measure the second order correlation, $g^{(2)}(0)$. Additionally, confinement within the DNH aperture may have an effect on the coherence and indistinguishability of the emitted photons which should be assessed with HOM interferometry [107]. Before performing these measurements, other factors that affect the coherence should be considered to yield the best results. One factor is Raman scattering which reduces the coherence as some energy is absorbed into the system. The excitation to the ${}^4I_{11/2}$ level with 980 nm light follows Stokes Raman scattering for the ${}^4I_{11/2} \rightarrow {}^4 I_{15/2}$ emission pathway, reducing the coherence of the emission [108]. Instead, excitation with 1480 nm can be used for the ${}^4I_{15/2} \leftrightarrow {}^4 I_{13/2}$ emission pathway as Rayleigh scattering preserves coherence [109]. Other coupling effects between the single emitter and the environment, such as electron-phonon and electron-plasmon, as well as the positioning of the nanoparticle and localized heating caused by the enhanced electric field, can have negative effects on the coherence of the emission [36], [110].

Selective anchoring of nanoparticles using a photochemical method with optical trapping is another novel technique that shows promise based on the preliminary results. While the experiment had a low overall yield, particularly for anchoring within the DNH, this was not unexpected for a novel method combining optical trapping with photochemistry. A similar anchoring method has been demonstrated previously using UV-triggered self-assembly with thiols in 'Click' chemistry, but this employs a significantly more complicated two-part reaction which also requires a surface-modified substrate [91]. Phototriggered reactions based on upconversion emission have also been used with surface-modified lanthanide-doped nanocrystals for biomedical applications, however it lacks the placement specificity required for our application [111]. The proposed photochemical anchoring method is comparatively simple and requires minimal sample preparation, and

would be an ideal if the yield can be improved.

A wide range of apertures, exposure times, and optical powers were used in the anchoring experiment, and by iteratively improving on the process, it is likely that the number of variables can be reduced. This preliminary work has shown that brief UV exposures are not sufficient to trigger anchoring, and that further tuning of the technique has promise to increase the yield. Additionally, as mentioned in the experiment, the trapping was performed using the polarization tuned for maximum transmission which is not consistent with prior work where the opposite polarization yielded maximum field intensity in the cusp region [100]. The other polarization should be explored as better placement specificity is required before this method can be considered functional. The emission of anchored particles may also vary if the device is used in air, and further investigation is needed to determine if the emission is comparable to the results seen for the hexane-dispersed nanocrystals of sections 4.1 and 4.2.

Fabricating nanoaperture optical fiber tweezers has been performed previously in our group, but the experiment presented in this thesis significantly lowers the cost by using colloidal pattern transfer rather than template stripping [53], [85]. Template stripping requires the DNHs to be produced with focused-ion beam milling which has significant costs but, as the attachment is an external process, this method could be reasonably scaled with many templates milled on each chip [53]. Other methods have used focused-ion beam milling to fabricate the DNH directly on the fiber, but this requires additional steps to etch the fiber core for alignment and it does not scale well as only a few fibers can be held within the machine for milling [52]. The colloidal pattern transfer method requires minimal fabrication time for the DNH samples, but is bottlenecked by the time to find suitable DNHs and the manual fiber attachment process.

This method relies on finding isolated DNHs in a sparse distribution, which is a

time consuming task regardless of whether SEM or polarization analysis is used to identify DNHs. Automation of this searching technique could result in a scalable and rapid search method. The stability and precision of the fabrication setup was also an issue during this experiment, constant manual adjustment was required to perform the fabrication steps while combating mechanical drift and backlash. This is acceptable for a lab environment but if this is to be made a truly accessible technology, major improvements will be necessary to ensure reliable production. While fabrication was a challenge, the fiber-based trapping setups used in this experiment showed promise as they required no adjustment or alignment to operate.

Overall, these techniques are effective but they have room for several improvements and the yields must be improved before moving to the next steps. Erbium-doped nanocrystals are a promising candidate for single photon sources which can be enhanced and isolated using DNH aperture optical trapping. The literature has also shown that erbium-doped nanocrystals have useful optical and quantum characteristics, but these need to be confirmed in a DNH. The initial results from the nanoparticle anchoring method showed that it can be used to anchor the surface-modified nanoparticles on the gold surface. The method suffered from limited control and low yield, but these both have potential avenues for improvement. Finally, the colloidal pattern transfer method showed that nanoaperture optical fiber tweezers can be produced for a low cost per attempt, but with significant time investment.

Chapter 6

Conclusion

This thesis has demonstrated a path towards a fiber integrated single photon source based on erbium-doped nanocrystals through four experiments which encompass a wide range of nanofabrication, photochemical, and optical trapping techniques. Employing nanoaperture optical trapping with DNHs allows for simultaneous isolation and enhancement of erbium-doped nanocrystals. This is built upon with a photochemical method intended to enable optically trapped nanoparticles to be selectively anchored within a DNH aperture. Finally, the colloidal pattern transfer method was presented as a low-cost fabrication method for nanoaperture optical fiber tweezers. This process can make nanoaperture optical trapping more accessible, and provides a platform for developing a fiber-coupled single photon source fabricated with optical trapping and photochemical anchoring.

The geometry of DNH apertures were shown to have a significant effect on the emission enhancement of optically trapped erbium-doped nanocrystals. This geometry was tuned to maximize the enhancement which showed improvement over rectangular apertures by a factor of 50. This enhancement allowed nanocrystals with discrete levels of active emitters to be detected and isolated in real-time. A novel photochemical anchoring method based on a UV-triggered thiol reaction showed 40% success for anchoring nanoparticles within 2 µm from DNHs, and 5% yield for anchoring within DNHs. This method still shows potential as future

works can further vary the range of parameters to develop the process. Finally, a colloidal pattern transfer method for producing integrated nanoaperture optical fiber tweezers was demonstrated. Optical trapping with a fiber-based setup was demonstrated using the nanoaperture optical fiber tweezers for 40 nm polystyrene and hBN. While the fabrication process proved to be challenging, the fiber-based trapping setup showed enormous utility with simplified sample preparation and no need for alignment.

The methods and experimental results presented in this thesis show significant promise and demonstrate a possible route to an integrated fiber-coupled single photon source. While the individual methods still need significant refinement before the final device can be realized, many of the advantages, shortcomings, and potential improvements for the methods have been envisaged. Additional future work to measure the photon statistics is of high importance as the characteristics of the actual device are critical for high-quality quantum control and communication. The development of an accessible fiber-coupled single photon source at 1550 nm would be a disruptive quantum technology, and these novel methods outline a potential path towards one which requires a focus on scaling and a directed effort to improve yields.

Bibliography

[1] Y.-A. Chen, Q. Zhang, T.-Y. Chen, W.-Q. Cai, S.-K. Liao, J. Zhang, K. Chen, J. Yin, J.-G. Ren, Z. Chen, S.-L. Han, Q. Yu, K. Liang, F. Zhou, X. Yuan, M.-S. Zhao, T.-Y. Wang, X. Jiang, L. Zhang, W.-Y. Liu, Y. Li, Q. Shen, Y. Cao, C.-Y. Lu, R. Shu, J.-Y. Wang, L. Li, N.-L. Liu, F. Xu, X.-B. Wang, C.-Z. Peng, and J.-W. Pan, "An integrated space-to-ground quantum communication network over 4,600 kilometres," *Nature*, pp. 1–6, Jan. 2021.

[2] M. M. Wilde, *Quantum Information Theory*, First. Cambridge: Cambridge University Press, 2013.

[3] J. Yin, Y.-H. Li, S.-K. Liao, M. Yang, Y. Cao, L. Zhang, J.-G. Ren, W.-Q. Cai, W.-Y. Liu, S.-L. Li, R. Shu, Y.-M. Huang, L. Deng, L. Li, Q. Zhang, N.-L. Liu, Y.-A. Chen, C.-Y. Lu, X.-B. Wang, F. Xu, J.-Y. Wang, C.-Z. Peng, A. K. Ekert, and J.-W. Pan, "Entanglement-based secure quantum cryptography over 1,120 kilometres," *Nature*, vol. 582, no. 7813, pp. 501–505, Jun. 2020.

[4] Y. Zhang, Z. Li, Z. Chen, C. Weedbrook, Y. Zhao, X. Wang, Y. Huang, C. Xu, X. Zhang, Z. Wang, M. Li, X. Zhang, Z. Zheng, B. Chu, X. Gao, N. Meng, W. Cai, Z. Wang, G. Wang, S. Yu, and H. Guo, "Continuous-variable QKD over 50 km commercial fiber," *Quantum Science and Technology*, vol. 4, no. 3, p. 035 006, May 2019.

[5] M. D. Eisaman, J. Fan, A. Migdall, and S. V. Polyakov, "Invited Review Article: Single-photon sources and detectors," *Review of Scientific Instruments*, vol. 82, no. 7, p. 071 101, Jul. 2011.

[6] N. Tomm, A. Javadi, N. O. Antoniadis, D. Najer, M. C. Löbl, A. R. Korsch, R. Schott, S. R. Valentin, A. D. Wieck, A. Ludwig, and R. J. Warburton, "A bright and fast source of coherent single photons," *Nature Nanotechnology*, Jan. 2021.

[7] E. Desurvire, *Erbium-Doped Fiber Amplifiers: Principles and Applications*. John Wiley and Sons, Inc., 1995.

[8] A. M. Dibos, M. Raha, C. M. Phenicie, and J. D. Thompson, "Atomic Source of Single Photons in the Telecom Band," *Physical Review Letters*, vol. 120, no. 24, p. 243 601, Jun. 2018.

[9] Y. Pang and R. Gordon, "Optical Trapping of 12 nm Dielectric Spheres Using Double-Nanoholes in a Gold Film," *Nano Letters*, vol. 11, no. 9, pp. 3763–3767, Sep. 2011.

[10] A. Alizadehkhaledi, A. L. Frencken, M. K. Dezfouli, S. Hughes, F. C. J. M. van Veggel, and R. Gordon, "Cascaded Plasmon-Enhanced Emission from a Single Upconverting Nanocrystal," *ACS Photonics*, vol. 6, no. 5, pp. 1125–1131, May 2019.

[11] J. F. Suyver, J. Grimm, M. K. van Veen, D. Biner, K. W. Krämer, and H. U. Güdel, "Upconversion spectroscopy and properties of NaYF4 doped with Er3+, Tm3+ and/or Yb3+," *Journal of Luminescence*, vol. 117, no. 1, pp. 1–12, Mar. 2006.

[12] Z. Sharifi, M. Dobinson, G. Hajisalem, M. S. Shariatdoust, A. L. Frencken, F. C. J. M. van Veggel, and R. Gordon, "Isolating and enhancing single-photon emitters for 1550 nm quantum light sources using double nanohole optical tweezers," *The Journal of Chemical Physics*, vol. 154, no. 18, p. 184 204, May 2021.

[13] A. Alizadehkhaledi, A. L. Frencken, F. C. J. M. van Veggel, and R. Gordon, "Isolating Nanocrystals with an Individual Erbium Emitter: A Route to a Stable Single-Photon Source at 1550 nm Wavelength," *Nano Letters*, vol. 20, no. 2, pp. 1018–1022, Feb. 2020.

[14] A. Laucht, F. Hohls, N. Ubbelohde, M. F. Gonzalez-Zalba, D. J. Reilly, S. Stobbe, T. Schröder, P. Scarlino, J. V. Koski, A. Dzurak, C.-H. Yang, J. Yoneda, F. Kuemmeth, H. Bluhm, J. Pla, C. Hill, J. Salfi, A. Oiwa, J. T. Muhonen, E. Verhagen, M. D. LaHaye, H. H. Kim, A. W. Tsen, D. Culcer, A. Geresdi, J. A. Mol, V. Mohan, P. K. Jain, and J. Baugh, "Roadmap on quantum nanotechnologies," *Nanotechnology*, vol. 32, no. 16, p. 162 003, Feb. 2021.

[15] M. E. Reimer and C. Cher, "The quest for a perfect single-photon source," *Nature Photonics*, vol. 13, no. 11, pp. 734–736, Nov. 2019.

[16] R. Gordon, "Metal Nanoapertures and Single Emitters," *Advanced Optical Materials*, p. 2 001 110, Aug. 2020.

[17] T. Zhong, J. M. Kindem, J. G. Bartholomew, J. Rochman, I. Craiciu, V. Verma, S. W. Nam, F. Marsili, M. D. Shaw, A. D. Beyer, and A. Faraon, "Optically Addressing Single Rare-Earth Ions in a Nanophotonic Cavity," *Physical Review Letters*, vol. 121, no. 18, p. 183 603, Oct. 2018.

[18] M Hennrich, T Legero, A Kuhn, and G Rempe, "Photon statistics of a non-stationary periodically driven single-photon source," *New Journal of Physics*, vol. 6, pp. 86–86, Jul. 2004.

[19] M. Steiner, A. Hartschuh, R. Korlacki, and A. J. Meixner, "Highly efficient, tunable single photon source based on single molecules," *Applied Physics Letters*, vol. 90, no. 18, p. 183 122, Apr. 2007.

[20] B. Lounis and W. E. Moerner, "Single photons on demand from a single molecule at room temperature," *Nature*, vol. 407, no. 6803, pp. 491–493, Sep. 2000.

[21] P. Senellart, G. Solomon, and A. White, "High-performance semiconductor quantum-dot single-photon sources," *Nature Nanotechnology*, vol. 12, no. 11, pp. 1026–1039, Nov. 2017.

[22] W. Redjem, A. Durand, T. Herzig, A. Benali, S. Pezzagna, J. Meijer, A. Y. Kuznetsov, H. S. Nguyen, S. Cueff, J.-M. Gérard, I. Robert-Philip, B. Gil, D. Caliste, P. Pochet, M. Abbarchi, V. Jacques, A. Dréau, and G. Cassabois, "Single artificial atoms in silicon emitting at telecom wavelengths," *Nature Electronics*, vol. 3, no. 12, pp. 738–743, Dec. 2020.

[23] S. Chen, Y.-A. Chen, T. Strassel, Z.-S. Yuan, B. Zhao, J. Schmiedmayer, and J.-W. Pan, "Deterministic and Storable Single-Photon Source Based on a Quantum Memory," *Physical Review Letters*, vol. 97, no. 17, p. 173 004, Oct. 2006.

[24] L. Novotny and B. Hecht, *Principles of Nano-Optics*. Cambridge University Press, 2012.

[25] C. H. Bennett, G. Brassard, C. Crépeau, R. Jozsa, A. Peres, and W. K. Wootters, "Teleporting an unknown quantum state via dual classical and Einstein-Podolsky-Rosen channels," *Physical Review Letters*, vol. 70, no. 13, pp. 1895–1899, Mar. 1993.

[26] C. H. Bennett and G. Brassard, "Quantum cryptography: Public key distribution and coin tossing," in *IEEE International Conference on Computers Systems and Signal Processing*, Bangalore, India, Dec. 1984, pp. 175–179.

[27] R. H. Brown and R. Twiss, "LXXIV. A new type of interferometer for use in radio astronomy," *The London, Edinburgh, and Dublin Philosophical Magazine and Journal of Science*, vol. 45, no. 366, pp. 663–682, Jul. 1954.

[28] C. K. Hong, Z. Y. Ou, and L. Mandel, "Measurement of subpicosecond time intervals between two photons by interference," *Physical Review Letters*, vol. 59, no. 18, pp. 2044–2046, Nov. 1987.

[29] Y. Tamura, H. Sakuma, K. Morita, M. Suzuki, Y. Yamamoto, K. Shimada, Y. Honma, K. Sohma, T. Fujii, and T. Hasegawa, "The First 0.14-dB/km Loss Optical Fiber and its Impact on Submarine Transmission," *Journal of Lightwave Technology*, vol. 36, no. 1, pp. 44–49, Jan. 2018.

[30] R. Kolesov, K. Xia, R. Reuter, R. Stöhr, A. Zappe, J. Meijer, P. Hemmer, and J. Wrachtrup, "Optical detection of a single rare-earth ion in a crystal," *Nature Communications*, vol. 3, no. 1, p. 1029, Jan. 2012.

[31] R. Kolesov, K. Xia, R. Reuter, M. Jamali, R. Stöhr, T. Inal, P. Siyushev, and J. Wrachtrup, "Mapping Spin Coherence of a Single Rare-Earth Ion in a Crystal onto a Single Photon Polarization State," *Physical Review Letters*, vol. 111, no. 12, p. 120 502, Sep. 2013.

[32] K. Xia, R. Kolesov, Y. Wang, P. Siyushev, R. Reuter, T. Kornher, N. Kukharchyk, A. D. Wieck, B. Villa, S. Yang, and J. Wrachtrup, "All-Optical Preparation of Coherent Dark States of a Single Rare Earth Ion Spin in a Crystal," *Physical Review Letters*, vol. 115, no. 9, p. 093 602, Aug. 2015.

[33] P. Siyushev, K. Xia, R. Reuter, M. Jamali, N. Zhao, N. Yang, C. Duan, N. Kukharchyk, A. D. Wieck, R. Kolesov, and J. Wrachtrup, "Coherent properties of single rare-earth spin qubits," *Nature Communications*, vol. 5, no. 1, p. 3895, Sep. 2014.

[34] S. Probst, H. Rotzinger, A. V. Ustinov, and P. A. Bushev, "Microwave multimode memory with an erbium spin ensemble," *Physical Review B*, vol. 92, no. 1, p. 014 421, Jul. 2015.

[35] T. Böttger, Y. Sun, C. W. Thiel, and R. L. Cone, "Spectroscopy and dynamics of Er 3 + : Y 2 Si O 5 at 1.5 μ m," *Physical Review B*, vol. 74, no. 7, p. 075 107, Aug. 2006.

[36] G. Liu and B. Jacquier, Eds., *Spectroscopic Properties of Rare Earths in Optical Materials*, ser. Springer Series in Materials Science. Berlin Heidelberg: Springer-Verlag, 2005.

[37] A. M. Dibos, M. Raha, C. M. Phenicie, and J. D. Thompson, *Isolating and enhancing the emission of single erbium ions using a silicon nanophotonic cavity*, 2017.

[38] U. Hohenester, *Nano and Quantum Optics: An Introduction to Basic Principles and Theory*, ser. Graduate Texts in Physics. Cham: Springer International Publishing, 2020.

[39] P. J. Schuck, D. P. Fromm, A. Sundaramurthy, G. S. Kino, and W. E. Moerner, "Improving the Mismatch between Light and Nanoscale Objects with Gold Bowtie Nanoantennas," *Physical Review Letters*, vol. 94, no. 1, p. 017 402, Jan. 2005.

[40] S. A. Maier, *Plasmonics: Fundamentals and Applications*. New York: Springer, 2007.

[41] D. M. Wu, A. García-Etxarri, A. Salleo, and J. A. Dionne, "Plasmon-Enhanced Upconversion," *The Journal of Physical Chemistry Letters*, vol. 5, no. 22, pp. 4020–4031, Nov. 2014.

[42] A. Teitelboim, B. Tian, D. J. Garfield, A. Fernandez-Bravo, A. C. Gotlin, P. J. Schuck, B. E. Cohen, and E. M. Chan, "Energy Transfer Networks within Upconverting Nanoparticles Are Complex Systems with Collective, Robust, and History-Dependent Dynamics," *The Journal of Physical Chemistry C*, vol. 123, no. 4, pp. 2678–2689, Jan. 2019.

[43] F. Wang, J. Wang, and X. Liu, "Direct Evidence of a Surface Quenching Effect on Size-Dependent Luminescence of Upconversion Nanoparticles," *Angewandte Chemie International Edition*, vol. 49, no. 41, pp. 7456–7460, 2010.

[44] B. Zhou, B. Shi, D. Jin, and X. Liu, "Controlling upconversion nanocrystals for emerging applications," *Nature Nanotechnology*, vol. 10, no. 11, pp. 924–936, Nov. 2015.

[45] D. Yuan, M. C. Tan, R. E. Riman, and G. M. Chow, "Comprehensive Study on the Size Effects of the Optical Properties of $NaYF_4$:Yb,Er Nanocrystals," *The Journal of Physical Chemistry C*, vol. 117, no. 25, pp. 13 297–13 304, Jun. 2013.

[46] K. Groot-Berning, T. Kornher, G. Jacob, F. Stopp, S. T. Dawkins, R. Kolesov, J. Wrachtrup, K. Singer, and F. Schmidt-Kaler, "Deterministic Single-Ion Implantation of Rare-Earth Ions for Nanometer-Resolution Color-Center Generation," *Physical Review Letters*, vol. 123, no. 10, p. 106 802, Sep. 2019.

[47] C. Santori, D. Fattal, J. Vučković, G. S. Solomon, and Y. Yamamoto, "Indistinguishable photons from a single-photon device," *Nature*, vol. 419, no. 6907, pp. 594–597, Oct. 2002.

[48] A. Ashkin, J. M. Dziedzic, J. E. Bjorkholm, and S. Chu, "Observation of a single-beam gradient force optical trap for dielectric particles," *Optics Letters*, vol. 11, no. 5, pp. 288–290, May 1986.

[49] M. L. Juan, R. Gordon, Y. Pang, F. Eftekhari, and R. Quidant, "Self-induced back-action optical trapping of dielectric nanoparticles," *Nature Physics*, vol. 5, no. 12, pp. 915–919, Dec. 2009.

[50] Y. Pang and R. Gordon, "Optical Trapping of a Single Protein," *Nano Letters*, vol. 12, no. 1, pp. 402–406, Jan. 2012.

[51] R. Gordon, "Biosensing with nanoaperture optical tweezers," *Optics & Laser Technology*, vol. 109, pp. 328–335, Jan. 2019.

[52] R. M. Gelfand, S. Wheaton, and R. Gordon, "Cleaved fiber optic double nanohole optical tweezers for trapping nanoparticles," *Optics Letters*, vol. 39, no. 22, p. 6415, Nov. 2014.

[53] J. M. Ehtaiba and R. Gordon, "Template-stripped nanoaperture tweezer integrated with optical fiber," *Optics Express*, vol. 26, no. 8, pp. 9607–9613, Apr. 2018.

[54] K. Okamoto and S. Kawata, "Radiation Force Exerted on Subwavelength Particles near a Nanoaperture," *Physical Review Letters*, vol. 83, no. 22, pp. 4534–4537, Nov. 1999.

[55] M. Nieto-Vesperinas, P. C. Chaumet, and A. Rahmani, "Near-field photonic forces," *Philosophical Transactions of the Royal Society of London. Series A: Mathematical, Physical and Engineering Sciences*, vol. 362, no. 1817, D. Richards and A. Zayats, Eds., pp. 719–737, Apr. 2004.

[56] L. Huang and O. J. F. Martin, "Reversal of the optical force in a plasmonic trap," *Optics Letters*, vol. 33, no. 24, p. 3001, Dec. 2008.

[57] L. Novotny, R. X. Bian, and X. S. Xie, "Theory of Nanometric Optical Tweezers," *Physical Review Letters*, vol. 79, no. 4, pp. 645–648, Jul. 1997.

[58] M. Righini, A. S. Zelenina, C. Girard, and R. Quidant, "Parallel and selective trapping in a patterned plasmonic landscape," *Nature Physics*, vol. 3, no. 7, pp. 477–480, Jul. 2007.

[59] M. Righini, G. Volpe, C. Girard, D. Petrov, and R. Quidant, "Surface Plasmon Optical Tweezers: Tunable Optical Manipulation in the Femtonewton Range," *Physical Review Letters*, vol. 100, no. 18, p. 186 804, May 2008.

[60] M. Righini, P. Ghenuche, S. Cherukulappurath, V. Myroshnychenko, F. J. García de Abajo, and R. Quidant, "Nano-optical Trapping of Rayleigh Particles and Escherichia coli Bacteria with Resonant Optical Antennas," *Nano Letters*, vol. 9, no. 10, pp. 3387–3391, Oct. 2009.

[61] E.-S. Kwak, T.-D. Onuta, D. Amarie, R. Potyrailo, B. Stein, S. C. Jacobson, W. L. Schaich, and B. Dragnea, "Optical Trapping with Integrated Near-Field Apertures," *The Journal of Physical Chemistry B*, vol. 108, no. 36, pp. 13 607–13 612, Sep. 2004.

[62] H. A. Bethe, "Theory of Diffraction by Small Holes," *Physical Review*, vol. 66, no. 7-8, pp. 163–182, Oct. 1944.

[63] C. Chen, M. L. Juan, Y. Li, G. Maes, G. Borghs, P. Van Dorpe, and R. Quidant, "Enhanced Optical Trapping and Arrangement of Nano-Objects in a Plasmonic Nanocavity," *Nano Letters*, vol. 12, no. 1, pp. 125–132, Dec. 2011.

[64] A. Kotnala and R. Gordon, "Quantification of High-Efficiency Trapping of Nanoparticles in a Double Nanohole Optical Tweezer," *Nano Letters*, vol. 14, no. 2, pp. 853–856, Feb. 2014.

[65] H. Xu, S. Jones, B.-C. Choi, and R. Gordon, "Characterization of Individual Magnetic Nanoparticles in Solution by Double Nanohole Optical Tweezers," *Nano Letters*, vol. 16, no. 4, pp. 2639–2643, Apr. 2016.

[66] M. U. Raza, S. S. S. Peri, L.-C. Ma, S. M. Iqbal, and G. Alexandrakis, "Self-induced back action actuated nanopore electrophoresis (SANE)," *Nanotechnology*, vol. 29, no. 43, p. 435 501, Aug. 2018.

[67] A. Kotnala, D. DePaoli, and R. Gordon, "Sensing nanoparticles using a double nanohole optical trap," *Lab on a Chip*, vol. 13, no. 20, pp. 4142–4146, Sep. 2013.

[68] R. A. Jensen, I.-C. Huang, O. Chen, J. T. Choy, T. S. Bischof, M. Lončar, and M. G. Bawendi, "Optical Trapping and Two-Photon Excitation of Colloidal Quantum Dots Using Bowtie Apertures," *ACS Photonics*, vol. 3, no. 3, pp. 423–427, Mar. 2016.

[69] J. Berthelot, S. S. Aćimović, M. L. Juan, M. P. Kreuzer, J. Renger, and R. Quidant, "Three-dimensional manipulation with scanning near-field optical nanotweezers," *Nature Nanotechnology*, vol. 9, no. 4, pp. 295–299, Apr. 2014.

[70] B. J. Roxworthy, K. D. Ko, A. Kumar, K. H. Fung, E. K. C. Chow, G. L. Liu, N. X. Fang, and K. C. Toussaint, "Application of Plasmonic Bowtie Nanoantenna Arrays for Optical Trapping, Stacking, and Sorting," *Nano Letters*, vol. 12, no. 2, pp. 796–801, Feb. 2012.

[71] E. Verhagen, L. Kuipers, and A. Polman, "Field enhancement in metallic subwavelength aperture arrays probed by erbium upconversion luminescence," *Optics Express*, vol. 17, no. 17, pp. 14 586–14 598, Aug. 2009.

[72] M. Saboktakin, X. Ye, U. K. Chettiar, N. Engheta, C. B. Murray, and C. R. Kagan, "Plasmonic Enhancement of Nanophosphor Upconversion Luminescence in Au Nanohole Arrays," *ACS Nano*, vol. 7, no. 8, pp. 7186–7192, Aug. 2013.

[73] Q. Jiang, B. Rogez, J.-B. Claude, G. Baffou, and J. Wenger, "Quantifying the Role of the Surfactant and the Thermophoretic Force in Plasmonic Nano-optical Trapping," *Nano Letters*, vol. 20, no. 12, pp. 8811–8817, Dec. 2020.

[74] C. Hong, S. Yang, and J. C. Ndukaife, "Stand-off trapping and manipulation of sub-10 nm objects and biomolecules using opto-thermo-electrohydrodynamic tweezers," *Nature Nanotechnology*, vol. 15, no. 11, pp. 908–913, Nov. 2020.

[75] S. S. S. Peri, M. K. Sabnani, M. U. Raza, E. L. Urquhart, S. Ghaffari, J. S. Lee, M. J. Kim, J. Weidanz, and G. Alexandrakis, "Quantification of low affinity binding interactions between natural killer cell inhibitory receptors and targeting ligands with a self-induced back-action actuated nanopore electrophoresis (SANE) sensor," *Nanotechnology*, vol. 32, no. 4, p. 045 501, Oct. 2020.

[76] D. Verschueren, X. Shi, and C. Dekker, "Nano-Optical Tweezing of Single Proteins in Plasmonic Nanopores," *Small Methods*, vol. 3, no. 5, p. 1 800 465, 2019.

[77] F. Eftekhari, C. Escobedo, J. Ferreira, X. Duan, E. M. Girotto, A. G. Brolo, R. Gordon, and D. Sinton, "Nanoholes As Nanochannels: Flow-through Plasmonic Sensing," *Analytical Chemistry*, vol. 81, no. 11, pp. 4308–4311, Jun. 2009.

[78] A. A. Al Balushi, A. Kotnala, S. Wheaton, R. M. Gelfand, Y. Rajashekara, and R. Gordon, "Label-free free-solution nanoaperture optical tweezers for

single molecule protein studies," *The Analyst*, vol. 140, no. 14, pp. 4760–4778, 2015.

[79] N. Hacohen, C. J. X. Ip, and R. Gordon, "Analysis of Egg White Protein Composition with Double Nanohole Optical Tweezers," *ACS Omega*, vol. 3, no. 5, pp. 5266–5272, May 2018.

[80] A. Kotnala and R. Gordon, "Double nanohole optical tweezers visualize protein p53 suppressing unzipping of single DNA-hairpins," *Biomedical Optics Express*, vol. 5, no. 6, p. 1886, Jun. 2014.

[81] A. A. Al Balushi, A. Zehtabi-Oskuie, and R. Gordon, "Observing single protein binding by optical transmission through a double nanohole aperture in a metal film," *Biomedical Optics Express*, vol. 4, no. 9, p. 1504, Sep. 2013.

[82] A. A. Al Balushi and R. Gordon, "A Label-Free Untethered Approach to Single-Molecule Protein Binding Kinetics," *Nano Letters*, vol. 14, no. 10, pp. 5787–5791, Oct. 2014.

[83] A. Zehtabi-Oskuie, H. Jiang, B. R. Cyr, D. W. Rennehan, A. A. Al-Balushi, and R. Gordon, "Double nanohole optical trapping: Dynamics and protein-antibody co-trapping," *Lab on a Chip*, vol. 13, no. 13, p. 2563, 2013.

[84] X. Zhao, N. Zhao, Y. Shi, H. Xin, and B. Li, "Optical Fiber Tweezers: A Versatile Tool for Optical Trapping and Manipulation," *Micromachines*, vol. 11, no. 2, p. 114, Jan. 2020.

[85] J. M. Ehtaiba and R. Gordon, "Beaming light through a bow-tie nanoaperture at the tip of a single-mode optical fiber," *Optics Express*, vol. 27, no. 10, p. 14 112, May 2019.

[86] T. Bürgi, "Properties of the gold–sulphur interface: From self-assembled monolayers to clusters," *Nanoscale*, vol. 7, no. 38, pp. 15 553–15 567, Sep. 2015.

[87] Y. Xue, X. Li, H. Li, and W. Zhang, "Quantifying thiol–gold interactions towards the efficient strength control," *Nature Communications*, vol. 5, no. 1, p. 4348, Jul. 2014.

[88] P. Klán, T. Šolomek, C. G. Bochet, A. Blanc, R. Givens, M. Rubina, V. Popik, A. Kostikov, and J. Wirz, "Photoremovable Protecting Groups in Chemistry and Biology: Reaction Mechanisms and Efficacy," *Chemical Reviews*, vol. 113, no. 1, pp. 119–191, Jan. 2013.

[89] C.-H. Park and R. S. Givens, "New Photoactivated Protecting Groups. 6. p-Hydroxyphenacyl:.1667em A Phototrigger for Chemical and Biochemical Probes1,2," *Journal of the American Chemical Society*, vol. 119, no. 10, pp. 2453–2463, Mar. 1997.

[90] R. S. Givens, J. F. W. Weber, P. G. Conrad, G. Orosz, S. L. Donahue, and S. A. Thayer, "New Phototriggers 9: *P* -Hydroxyphenacyl as a C-Terminal Photoremovable Protecting Group for Oligopeptides," *Journal of the American Chemical Society*, vol. 122, no. 12, pp. 2687–2697, Mar. 2000.

[91] D. Walker, D. P. Singh, and P. Fischer, "Capture of 2D Microparticle Arrays via a UV-Triggered Thiol-yne "Click" Reaction," *Advanced Materials*, vol. 28, no. 44, pp. 9846–9850, 2016.

[92] G. Hajisalem, E. Babaei, M. Dobinson, S. Iwamoto, Z. Sharifi, J. Eby, M. Synakewicz, L. S. Itzhaki, and R. Gordon, "Accessible high-performance double nanohole tweezers," *Optics Express*, vol. 30, no. 3, p. 3760, Jan. 2022.

[93] A. L. Ravindranath, M. S. Shariatdoust, S. Mathew, and R. Gordon, "Colloidal lithography double-nanohole optical trapping of nanoparticles and proteins," *Optics Express*, vol. 27, no. 11, p. 16 184, May 2019.

[94] S Swann, "Magnetron sputtering," *Physics in Technology*, vol. 19, no. 2, pp. 67–75, Mar. 1988.

[95] Z. Li and Y. Zhang, "An efficient and user-friendly method for the synthesis of hexagonal-phase NaYF $_4$:Yb, Er/Tm nanocrystals with controllable shape and upconversion fluorescence," *Nanotechnology*, vol. 19, no. 34, p. 345 606, Aug. 2008.

[96] H. Wang, X. Yin, M. Xing, Y. Fu, Y. Tian, X. Feng, T. Jiang, and X. Luo, "Thermal effects of Er3+/Yb3+ -doped NaYF4 phosphor induced by 980/1510 nm laser diode irradiation," *Journal of the American Ceramic Society*, vol. 101, no. 2, pp. 865–873, Feb. 2018.

[97] J. J. H. A. van Hest, G. A. Blab, H. C. Gerritsen, C. de Mello Donega, and A. Meijerink, "The Role of a Phonon Bottleneck in Relaxation Processes for Ln-Doped NaYF4 Nanocrystals," *The Journal of Physical Chemistry C*, vol. 122, no. 7, pp. 3985–3993, Feb. 2018.

[98] A. Lesuffleur, L. K. S. Kumar, and R. Gordon, "Enhanced second harmonic generation from nanoscale double-hole arrays in a gold film," *Applied Physics Letters*, vol. 88, no. 26, p. 261 104, Jun. 2006.

[99] A. Lesuffleur, L. K. S. Kumar, A. G. Brolo, K. L. Kavanagh, and R. Gordon, "Apex-Enhanced Raman Spectroscopy Using Double-Hole Arrays in a Gold Film," *The Journal of Physical Chemistry C*, vol. 111, no. 6, pp. 2347–2350, Feb. 2007.

[100] R. Regmi, A. A. Al Balushi, H. Rigneault, R. Gordon, and J. Wenger, "Nanoscale volume confinement and fluorescence enhancement with double nanohole aperture," *Scientific Reports*, vol. 5, no. 1, p. 15 852, Dec. 2015.

[101] J. C. Love, L. A. Estroff, J. K. Kriebel, R. G. Nuzzo, and G. M. Whitesides, "Self-Assembled Monolayers of Thiolates on Metals as a Form of Nanotechnology," *Chemical Reviews*, vol. 105, no. 4, pp. 1103–1170, Apr. 2005.

[102] M. S. Inkpen, Z.-F. Liu, H. Li, L. M. Campos, J. B. Neaton, and L. Venkataraman, "Non-chemisorbed gold–sulfur binding prevails in self-assembled monolayers," *Nature Chemistry*, vol. 11, no. 4, pp. 351–358, Apr. 2019.

[103] N. J. Brewer, R. E. Rawsterne, S. Kothari, and G. J. Leggett, "Oxidation of Self-Assembled Monolayers by UV Light with a Wavelength of 254 nm," *Journal of the American Chemical Society*, vol. 123, no. 17, pp. 4089–4090, May 2001.

[104] M. Lewis, M. Tarlov, and K. Carron, "Study of the Photooxidation Process of Self-Assembled Alkanethiol Monolayers," *Journal of the American Chemical Society*, vol. 117, no. 37, pp. 9574–9575, Sep. 1995.

[105] J. M. Ehtaiba, "An Integrated Nanoaperture Optical-Fiber Tweezer for Developing Single-Photon Sources," Ph.D. dissertation, 2020.

[106] O. Loebich, "The optical properties of gold: A review of their technical utilisation," *Gold Bulletin*, vol. 5, no. 1, pp. 2–10, Mar. 1972.

[107] F. Bouchard, A. Sit, Y. Zhang, R. Fickler, F. M. Miatto, Y. Yao, F. Sciarrino, and E. Karimi, "Two-photon interference: The Hong-Ou-Mandel effect," *Reports on Progress in Physics*, vol. 84, no. 1, p. 012 402, Jan. 2021.

[108] R. Ozeri, W. M. Itano, R. B. Blakestad, J. Britton, J. Chiaverini, J. D. Jost, C. Langer, D. Leibfried, R. Reichle, S. Seidelin, J. H. Wesenberg, and D. J. Wineland, "Errors in trapped-ion quantum gates due to spontaneous photon scattering," *Physical Review A*, vol. 75, no. 4, p. 042 329, Apr. 2007.

[109] R. Ozeri, C. Langer, J. Jost, B. DeMarco, A. Ben-Kish, B. Blakestad, J. Britton, J. Chiaverini, W. Itano, D. Hume, D. Leibfried, T. Rosenband, P. Schmidt, and D. Wineland, "Hyperfine Coherence in the Presence of Spontaneous Photon Scattering," *Physical Review Letters*, vol. 95, no. 3, p. 030 403, Jul. 2005.

[110] L. Mandel and E. Wolf, *Optical Coherence and Quantum Optics*. Cambridge ; New York: Cambridge University Press, 1995.

[111] S. Wu and H.-J. Butt, "Near-infrared photochemistry at interfaces based on upconverting nanoparticles," *Physical Chemistry Chemical Physics*, vol. 19, no. 35, pp. 23 585–23 596, 2017.

Appendices

Appendix A

Appendix A: UV Light Timing Program

To accurately control the UV source, a short program was written. This program allows the user to turn on the UV source for a specified duration and the circuit allows this to be measured by the DAQ so that the APD signal can be analyzed for the period during which the UV source is on.

A.1 Hardware

The lighting source consists of two LEDs, one UV and one green LED. The green LED is used to illuminate the sample to find the DNHs and perform trapping. A green LED is used rather than a white LED to avoid accidental triggering of the photochemical reaction.

Figure A.1 shows the schematic of the UV light timing circuit. A microcontroller (Arduino Uno) controls the UV LED using a transistor output circuit. The microcontroller interfaces with a PC for control over serial. A DAQ is used to monitor the UV LED voltage so that it can be synchronized with the APD signal, which is collected by the same DAQ.

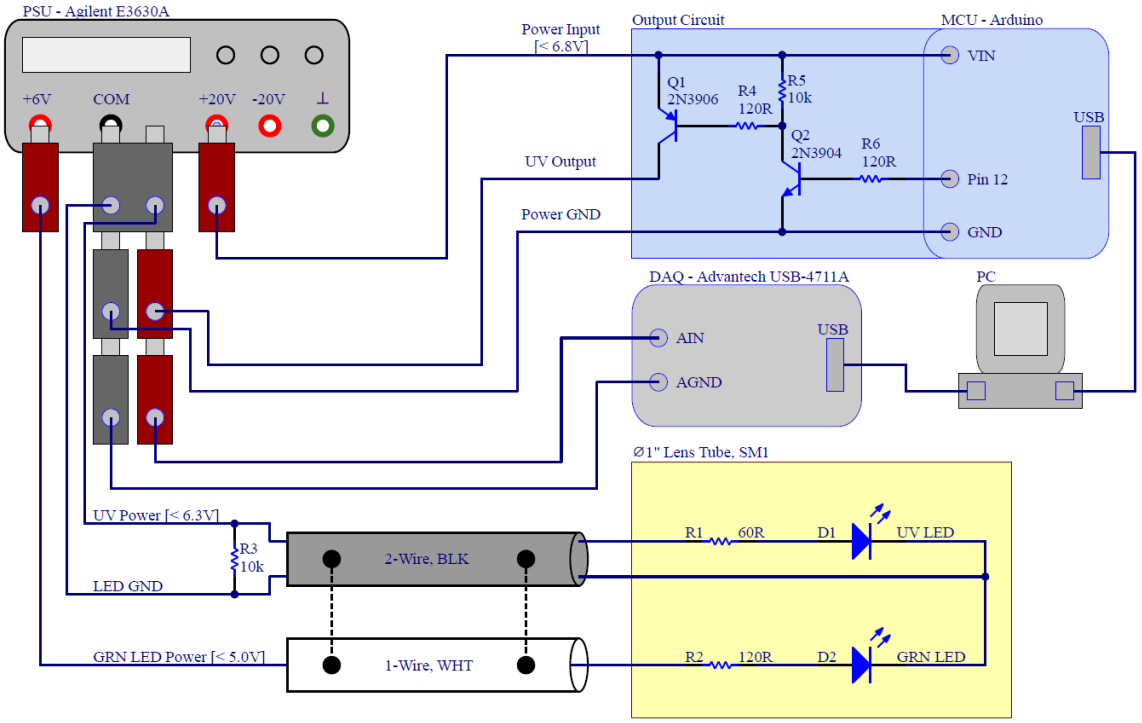

FIGURE A.1: Schematic of the UV timing circuitry and external connections.

A.2 Program Code

LISTING A.1: Timed Output Program

```
/*
*  Timed Output
*  created 15 June 2021 | modified 16 January 2022
*  by Michael Dobinson
*
*  Turns the output pin on for the amount of time specified by the
*  user over the serial port.
*
*  Procedure:
*  1. Connect to Arduino board over serial port @ 9600 baud
*  2. Wait for message "Connected." from Arduino
*  3. Send a blank message to establish connection, e.g. " "
*  4. Send a number in seconds to turn on the output pins for that
*   duration, e.g. "12.6"
```

```
15 *  5. Output pins will turn on for the specified duration
   and you
16 *   will receive a confirmation message, e.g. "LED ON for
   12.6s
17 *  6. Repeat from step 4 for additonal timed outputs
18 *
19 *  Note: Terminal must be set to output newline "\n" on
   enter
20 */
21
22 // initialization, runs on reset
23 void setup() {
24   Serial.begin(9600); // start serial @ 9600 baud
25
26   while (!Serial) { // wait to connect
27     ; // do nothing
28   }
29
30   // initialize pins 12 & 13 (LED_BUILTIN) as outputs.
31   pinMode(12, OUTPUT);
32   pinMode(LED_BUILTIN, OUTPUT);
33
34   // send messages until first response is received
35   establishContact();
36 }
37
38 void loop() {
39   // wait for user input over serial
40   if (Serial.available() > 0) {
41     String str = Serial.readString();   // get incoming byte
42
43     if(str.indexOf("\n") > -1){     // check message content
44       float num = str.toFloat();    // convert user string
            to float
45       Serial.print("LED ON for ");    // respond to user
46       Serial.print(num);
47       Serial.println("s");
48
49     // set output pins HIGH for the duration specified (if
        >10us)
50       if(num > 0.00001){
51         unsigned long startTime = millis(); // start timer
52         while(millis() - startTime <= num*1000)
53         {
```

```
54          // turn on outputs (HIGH)
55            digitalWrite(LED_BUILTIN, HIGH);
56            digitalWrite(12, HIGH);
57          }
58      // turn off outputs (LOW) after duration elapsed
59          digitalWrite(LED_BUILTIN, LOW);
60          digitalWrite(12, LOW);
61        }
62      }else{
63      // message invalid, send "unknown"
64        Serial.println("unknown");
65      }
66    }
67  }
68  // send a string to establish contact until receiver
       responds
69  void establishContact() {
70    while (Serial.available() <= 0) {
71      Serial.println("Connected.");   // send an initial
           string
72      delay(300);
73    }
74  }
```

A.3 Example Commands

Below is the example input/output for turning on the UV LED for 10.5s. The Arduino sends the following message every 300ms until user input is received:

```
>   Connected.
```

Begin connection by sending a message, this should be blank. After establishing a connection, send the duration you would like to turn on the outputs for, e.g. 10.5s:

```
>   Blank Message
>   10.5
```

The Arduino will respond and turn on the output for the specified duration:

```
>   LED ON for 10.5s
```